

TECHNICAL MEMORANDUM

X-365

Declassified by authority of NASA
Classification Change Notices No. 215
Dated **12/31/71TRANSONIC CHARACTERISTICS OF A SPACE VEHICLE
AND A MULTIPLE-STAGE ROCKET ASSEMBLY

By Roy M. Wakefield and Stuart L. Treon

Ames Research Center
Moffett Field, Calif.

UNCLASSIFIED

By Authority of 10.71-635 10/18/71

N71-75827

FACILITY FORM 602

(ACCESSION NUMBER)

51

(PAGES)

(NASA CR OR TMX OR AD NUMBER)

(THRU)

none

(CODE)

(CATEGORY)

NATIONAL AERONAUTICS AND SPACE ADMINISTRATION
WASHINGTON

August 1960

NATIONAL AERONAUTICS AND SPACE ADMINISTRATION

TECHNICAL MEMORANDUM X-365

TRANSONIC CHARACTERISTICS OF A SPACE VEHICLE

AND A MULTIPLE-STAGE ROCKET ASSEMBLY*

By Roy M. Wakefield and Stuart L. Treon

SUMMARY

An investigation in a transonic wind tunnel has been conducted to determine the static aerodynamic characteristics of models of a final-stage space vehicle and a multiple-stage rocket assembly. The final-stage models, which were nose-body-flare configurations, were tested to determine the effect of nose shape and the effect of the presence of the rocket booster. The rocket-assembly models were tested to determine the effect of asymmetric protuberances attached to the booster and the effect of roll angle. Reynolds number for the final-stage models was 0.58 million based on body diameter, and for the rocket-assembly models was 0.62 million based on the booster diameter. The angle-of-attack and Mach number ranges were about -4° to $+11^{\circ}$, and 0.4 to 1.4, respectively. The results are presented without discussion.

INTRODUCTION

The launch configuration of a multiple-stage rocket assembly must pass through the transonic speed range in the course of a mission. It is necessary to know the aerodynamic forces on the final stage in the presence of the other stages in order to determine the structural requirements at transonic speeds and to know the aerodynamic characteristics of the complete launch configuration in order to predict its behavior in transonic flight.

The present investigation of a multiple-stage rocket configuration was conducted in a transonic wind tunnel (1) to determine the static aerodynamic characteristics of the final-stage vehicle, (2) to assess the effect of the presence of the booster rocket on the aerodynamic characteristics of the final-stage vehicle, and (3) to measure the static aerodynamic characteristics of the complete rocket assembly. The results are presented without discussion.

NOTATION

C_A	forebody axial-force coefficient, $\frac{\text{forebody axial force}}{qS}$
C_l	rolling-moment coefficient, $\frac{\text{rolling moment}}{qSd}$
C_m	pitching-moment coefficient about moment reference (see figs. 1 and 2(a)), $\frac{\text{pitching moment}}{qSd}$
C_N	normal-force coefficient, $\frac{\text{normal force}}{qS}$
C_n	yawing-moment coefficient about moment reference (see fig. 2(a)), $\frac{\text{yawing moment}}{qSd}$
C_Y	side-force coefficient, $\frac{\text{side force}}{qS}$
$\frac{C_m}{\alpha}$	slope of the straight line drawn from C_m at $\alpha = 0^\circ$ to any point on the C_m vs. α curve
$\frac{C_N}{\alpha}$	slope of the straight line drawn from C_N at $\alpha = 0^\circ$ to any point on the C_N vs. α curve
c.p.	center of pressure, $\frac{C_m/\alpha}{C_N/\alpha}$, diameters from moment reference
d	vehicle or booster cylindrical body diameter
M	Mach number
q	dynamic pressure
S	cylindrical body cross-sectional area of vehicle or booster
α	angle of attack, deg
ϕ	angle or roll, deg

APPARATUS AND MODELS

The investigation was conducted in the Ames 2-by 2-Foot Transonic Wind Tunnel which is of the closed-circuit, variable-pressure type. This facility has a perforated test section which permits continuous choke-free operation at Mach numbers up to 1.4. Additional details regarding this facility are presented in reference 1.

A
2
6
1

The models (figs. 1 and 2) were three final-stage vehicles mounted ahead of a booster rocket foresection (1-VB, 2-VB, 3-VB), a final-stage vehicle without the booster rocket (1-V), and two multiple-stage rocket assemblies (4-A, 5-A). The final-stage vehicles differed primarily in nose shape, the shapes being a round-nosed cone, a hemisphere, and a spherical segment of large radius (the length of the models varied from 3.5 to 4.2 body diameters). The booster foresection was mounted on the model support sting, independent of the balance and final-stage model (fig. 1(a)). An electrical device was used to indicate any contact between the final-stage model and the booster foresection. The rocket-assembly models (fig. 2) were identical except for the external fairings on the booster. Details of the fairings are shown in figure 2(b). The rocket-assembly models were 8.7 booster diameters long and incorporated an appropriately scaled final-stage vehicle with the blunted conical nose (1-V). The model roll angle was measured from the stationary positive normal-force plane of the balance to the center line of fairings 1 and 2 as shown in figure 2(a).

The models were mounted in the wind-tunnel test section on a sting-supported strain-gage balance of the type shown in reference 1. Photographs of two of the models are shown in figure 3.

TESTS

The tests were conducted at angles of attack from about -4° to $+11^\circ$ at Mach numbers from 0.4 to 1.4. The Reynolds number for the final-stage models was 0.58 million referred to the model body diameter, and for the rocket-assembly models was 0.62 million referred to the booster body diameter. Model roll angles were 0° only for model 4-A, and 0° , 45° , 90° , and 180° for model 5-A.

Boundary-layer trip wires were attached to the conical noses of models 1-V, 1-VB, 4-A, and 5-A, as shown in figures 1(a) and 2(a). The wires were used to insure transition on the forepart of the noses and to minimize the variation in the location of transition on these models. The trip wires were located in regions where transition would likely

occur at Reynolds numbers of full-scale flight. The wires are believed to have been effective on the basis of observations of the flow over similar models of reference 2 at test conditions comparable to those of the present investigation. For models with more blunt noses, such as 2-VB and 3-VB, little information is available regarding the flow conditions at high Reynolds numbers at transonic speeds. However, in some unpublished shadowgraphs of a blunt-nosed model in the Ames Supersonic Free-Flight Range at Reynolds numbers of about 6.5 million at transonic speeds, there is evidence of extensive laminar flow on the model nose. Therefore, models 2-VB and 3-VB were tested without trip wires in order not to interfere with the flow over the model noses.

DATA REDUCTION

The data were reduced to coefficient form referred to the body axes using the reference areas and lengths indicated in figures 1 and 2. For the forebody coefficients, the measured axial forces were adjusted to account for the difference between the base pressures and an assumed condition of free-stream static pressure acting at the base of the model.

The angles of attack were corrected for deflection of the balance and sting under aerodynamic loads. Stream-angularity corrections are negligible. No corrections have been made for possible interference effects of the perforated test-section walls. Such effects are believed to be small in view of the results of tests of sharp- and blunt-nosed bodies reported in the appendix to reference 2.

In addition to the possible systematic errors resulting from neglecting some of the above effects, certain random errors exist which influence the precision, or repeatability, of the results. The estimated average deviations of values of Mach number, angle of attack, and the aerodynamic coefficients were as follows:

M	± 0.003	C_A	± 0.012
α	$\pm 0.1^\circ$	C_Y	± 0.002
C_N	± 0.004	C_n	± 0.004
C_m	± 0.004	C_l	± 0.004

RESULTS

Results of the investigation are presented as follows:

Models	Data presented	Figures
1-VB, 2-VB, and 3-VB	C_N , C_m , and C_A vs. α $\frac{C_N}{\alpha}$, c.p., and $C_{A_{\alpha=0^\circ}}$ vs. M	4 through 9
1-VB and 1-V	C_N , C_m , and C_A vs. α $\frac{C_N}{\alpha}$, c.p., and $C_{A_{\alpha=0^\circ}}$ vs. M	10 through 15
4-A and 5-A	C_N , C_m , C_A , C_y , C_n , and C_l vs. α $\frac{C_N}{\alpha}$, c.p., and $C_{A_{\alpha=0^\circ}}$ vs. M	16 through 24

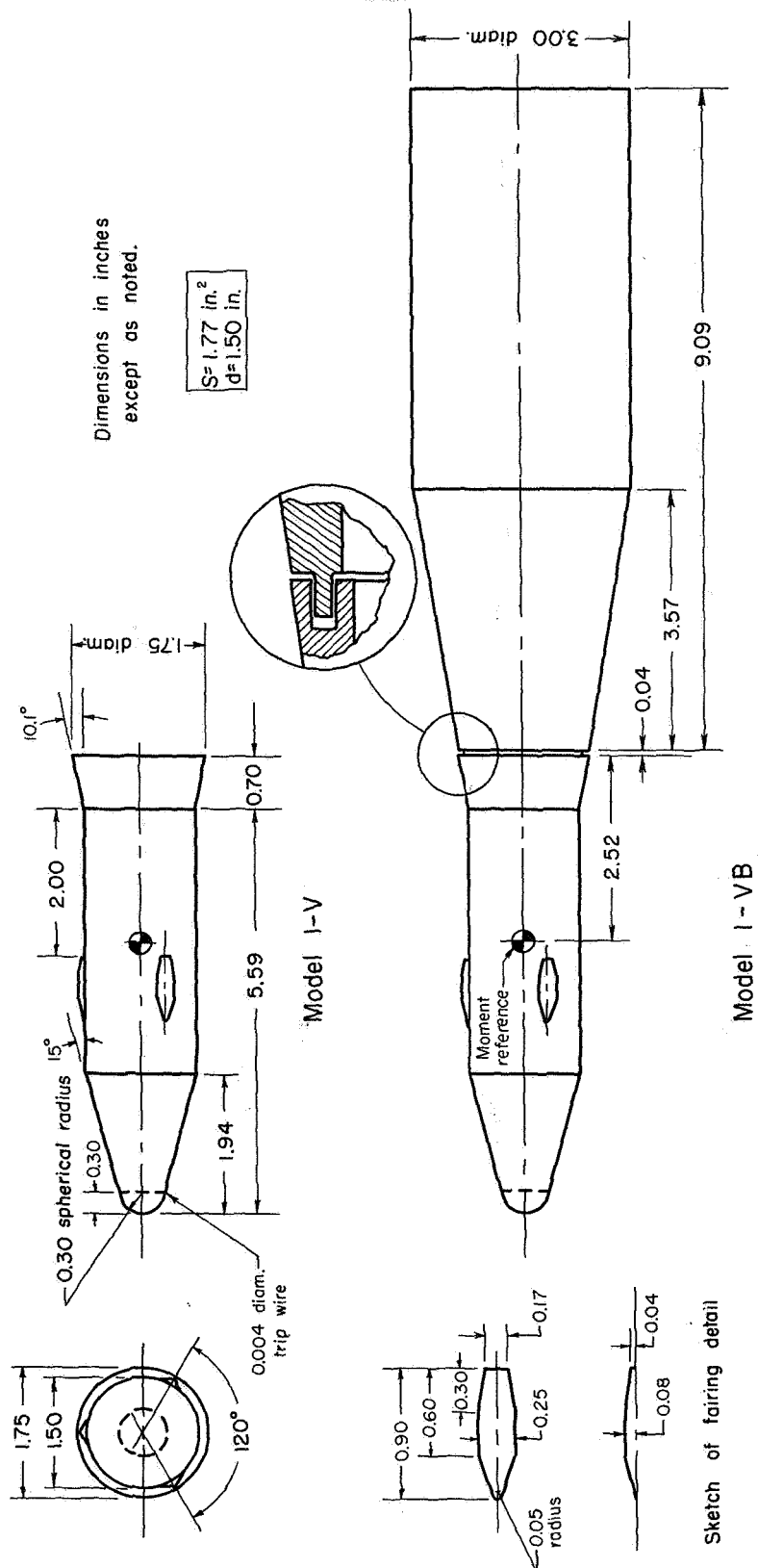
Aerodynamic hysteresis has been observed for blunt-nosed bodies (refs. 3 and 4) similar to the final-stage model 3-VB. The hysteresis, which is associated with separated flow, can be detected by increasing and then decreasing angle of attack over a particular angle range. The occurrence of hysteresis for the models of this investigation was not determined, since data were obtained for increasing α only. However, on the basis of results presented in reference 4, aerodynamic hysteresis would not be expected on models 1-VB or 2-VB.

Ames Research Center

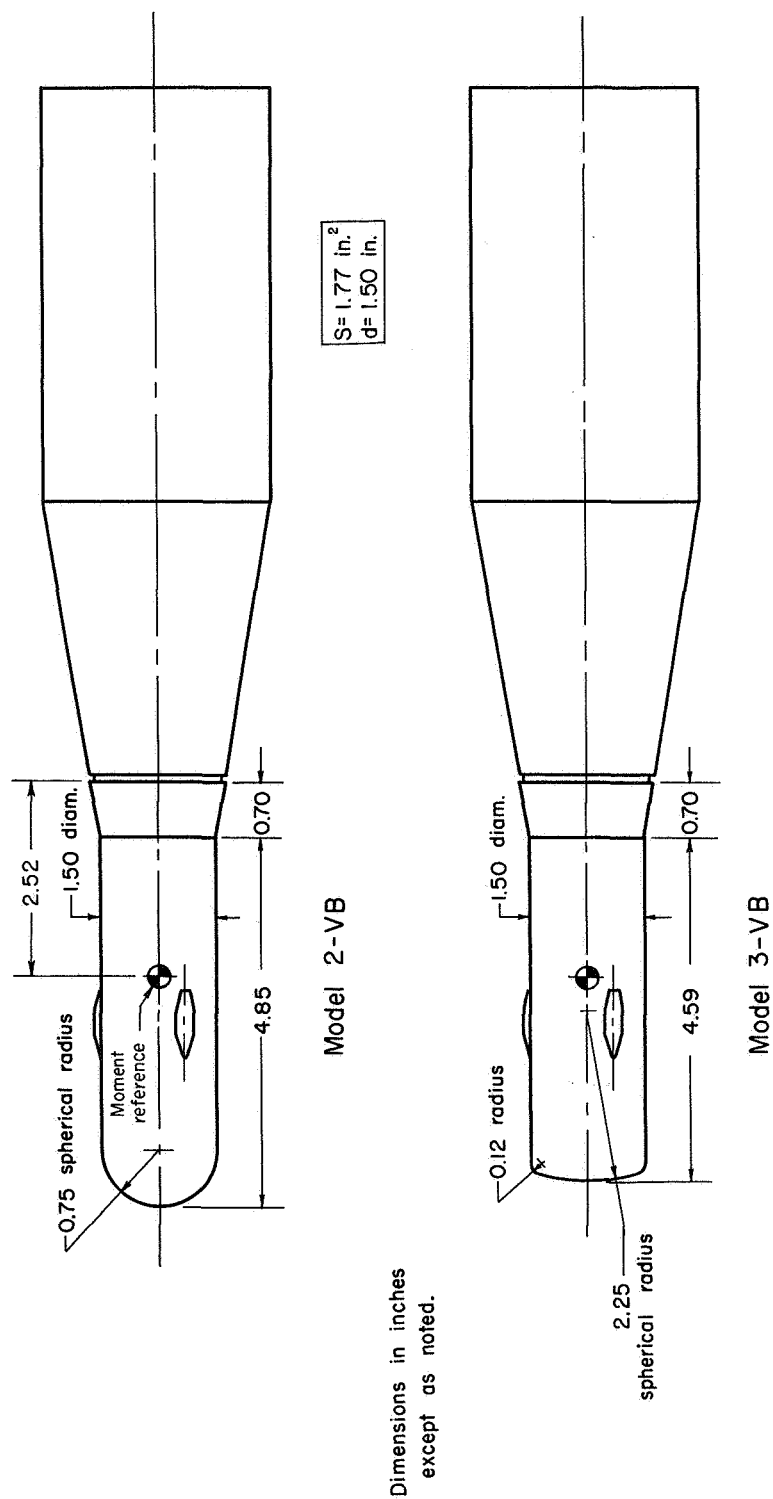
National Aeronautics and Space Administration
Moffett Field, Calif., Feb. 8, 1960

REFERENCES

1. Spiegel, Joseph M., and Lawrence, Leslie F.: A Description of the Ames 2- by 2-Foot Transonic Wind Tunnel and Preliminary Evaluation of Wall Interference. NACA RM A55I21, 1956.
2. Treon, Stuart L.: The Effect of Nose Shape on the Static Aerodynamic Characteristics of Ballistic-Type Missile Models at Mach Numbers From 0.6 to 1.4. NASA MEMO 5-17-59A, 1959.
3. Reese, David E., Jr., and Wehrend, William R., Jr.: An Investigation of the Static and Dynamic Aerodynamic Characteristics of a Series of Blunt Nosed Cylinder-Flare Models at Mach Numbers From 0.65 to 2.20. NASA TM X-110, 1959.
4. Treon, Stuart L., Wakefield, Roy M., and Knechtel, Earl D.: Effects of Nose Shape and Afterbody Flare on the Transonic Characteristics of a Low-Fineness-Ratio Body of Revolution. NASA TM X-164, 1960.

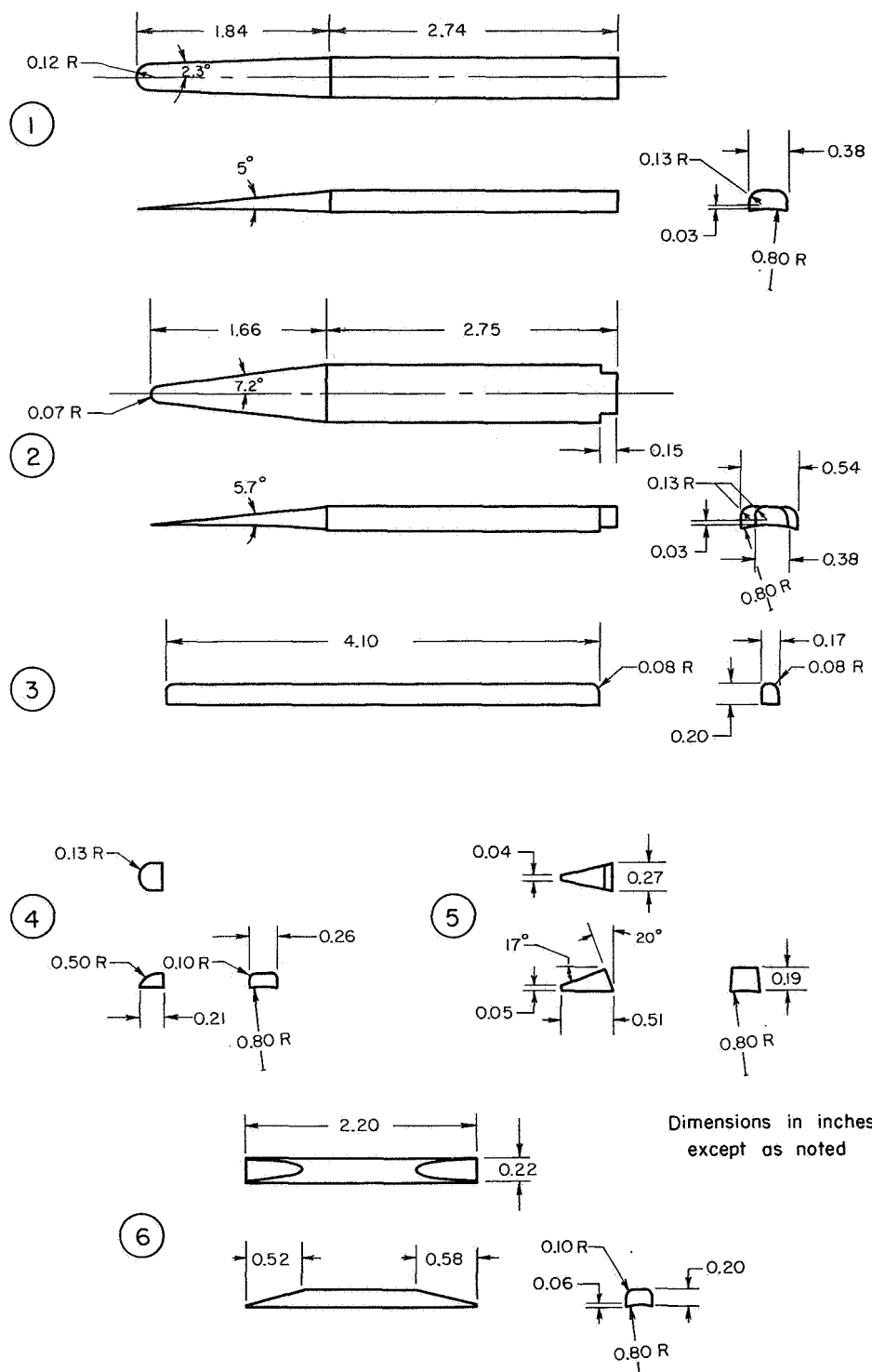


(a) Details of models 1-V and 1-VB.
Figure 1.- Dimensioned sketches of final-stage vehicle models and the body simulating the booster rocket.



(b) Details of models 2-VB and 3-VB.

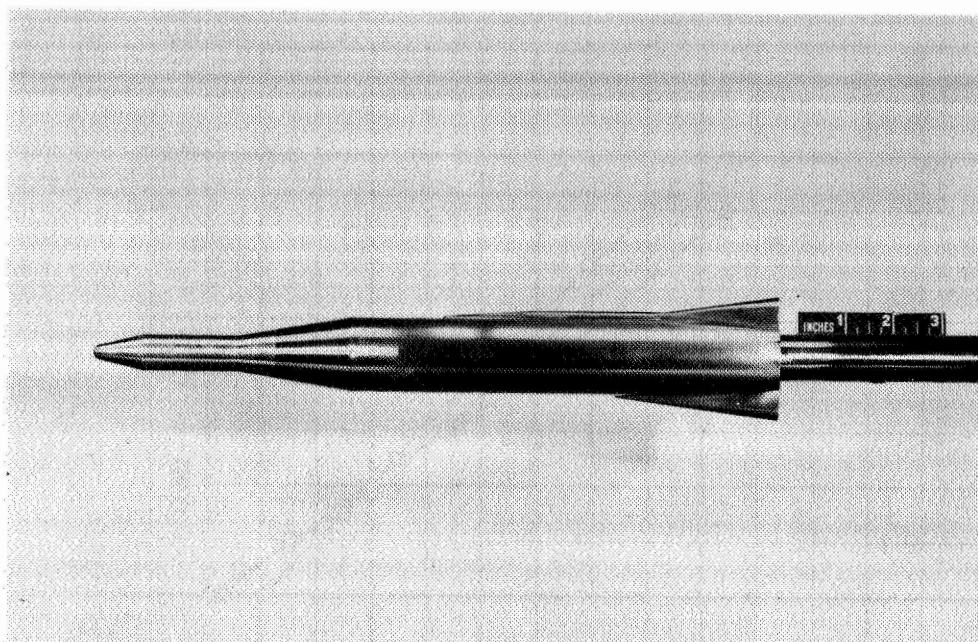
Figure 1.- Concluded.



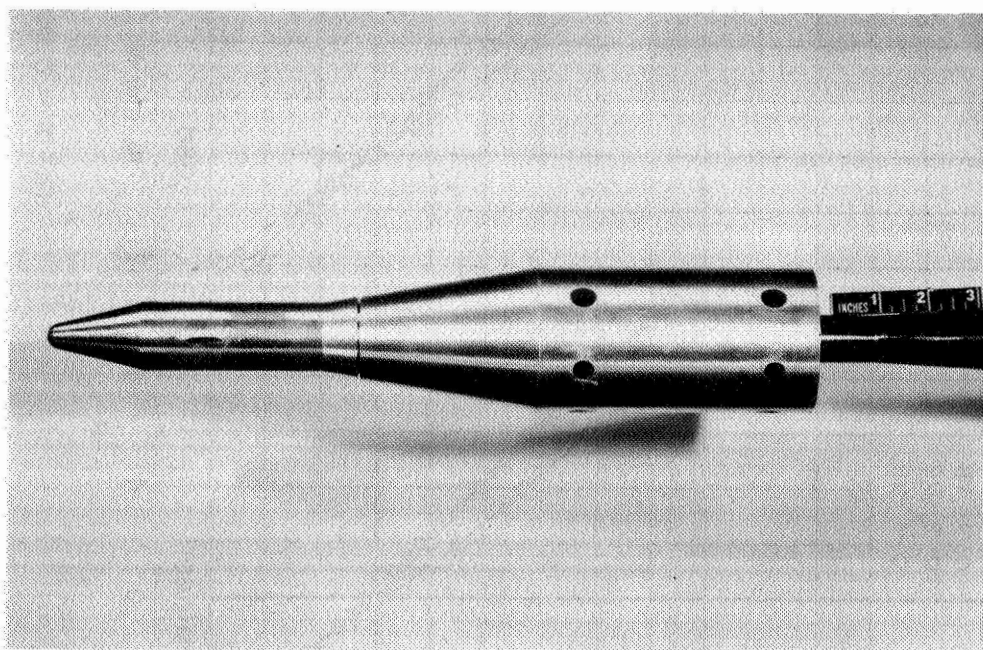
(b) Details of protuberances attached to models 4-A and 5-A.

Figure 2.- Concluded.

A
2
6
1

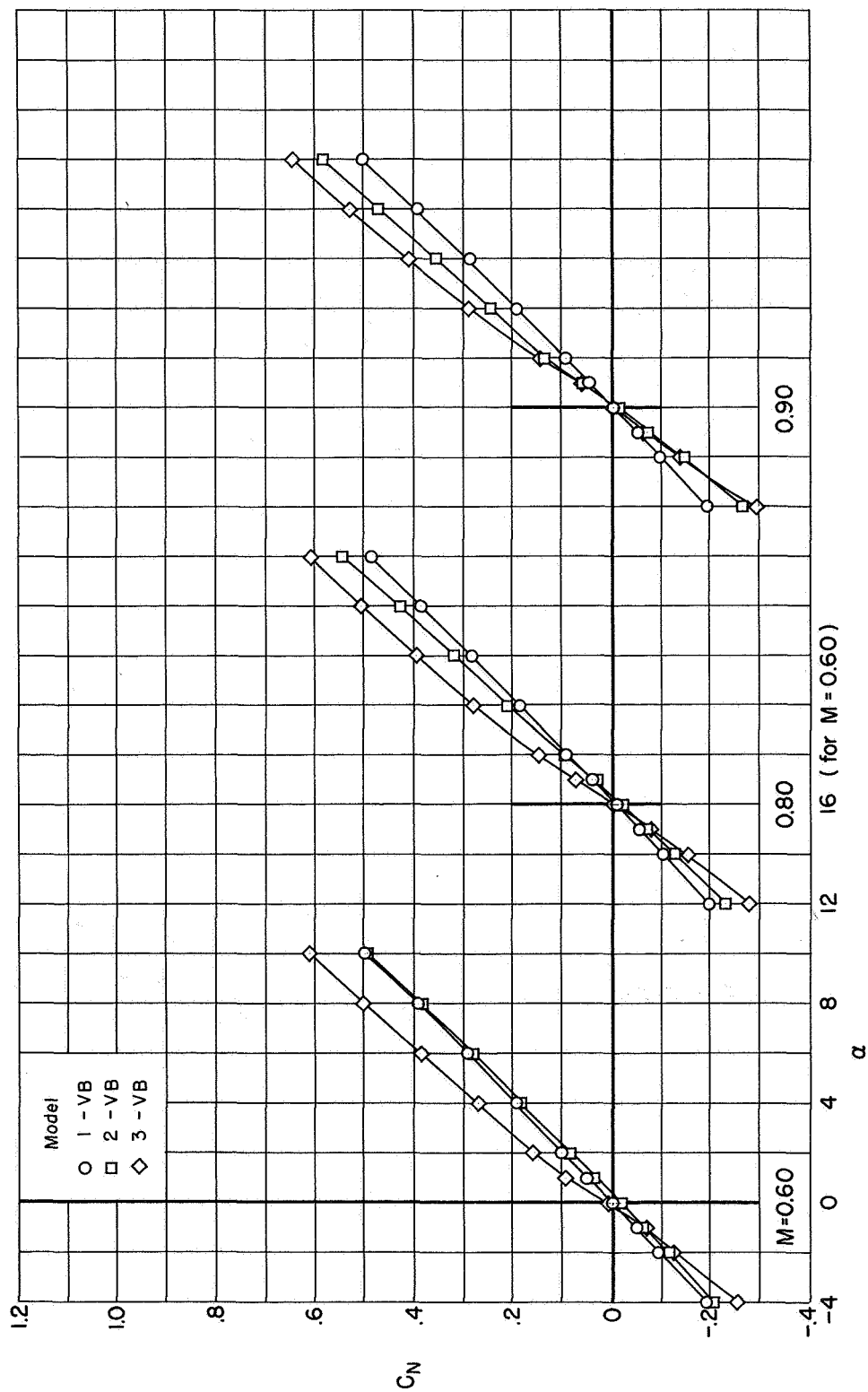


(b) Model 4-A.



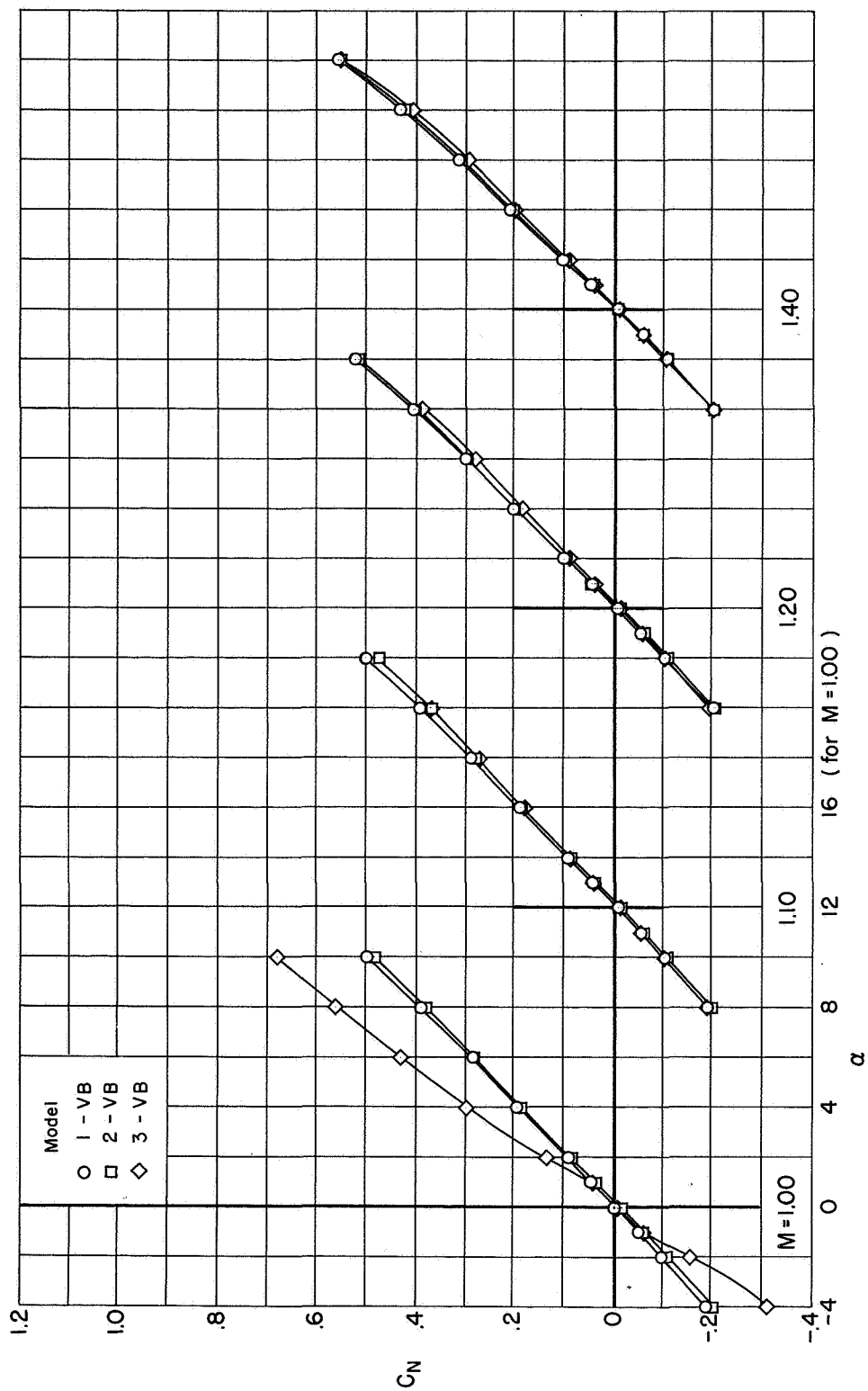
(a) Model 1-VB.

Figure 3.- Typical models employed in the investigation.



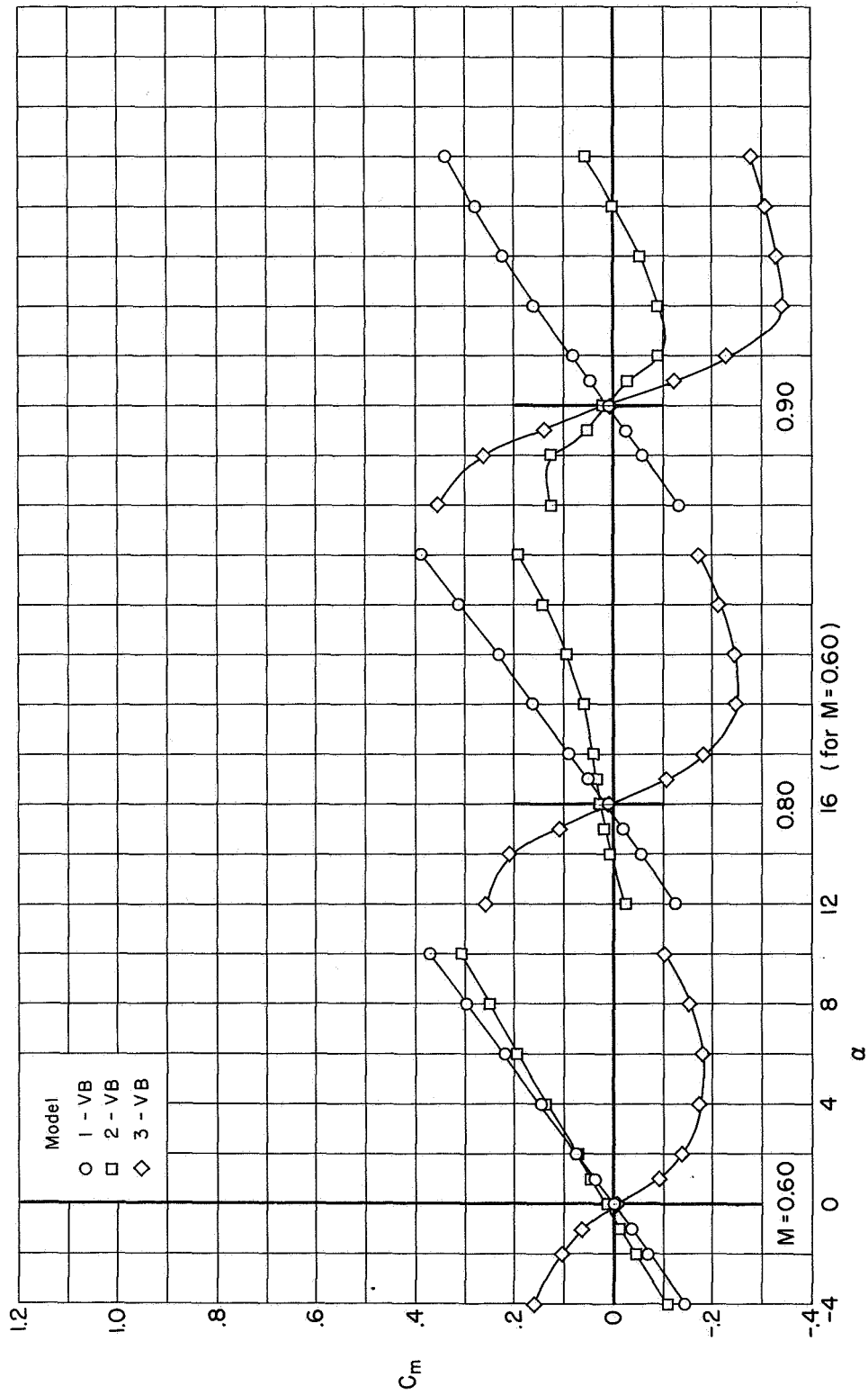
(a) $M = 0.60$ to 0.90

Figure 4.- Effect of vehicle nose-shape on the variation of normal-force coefficient for vehicle models in the presence of a simulated booster rocket.



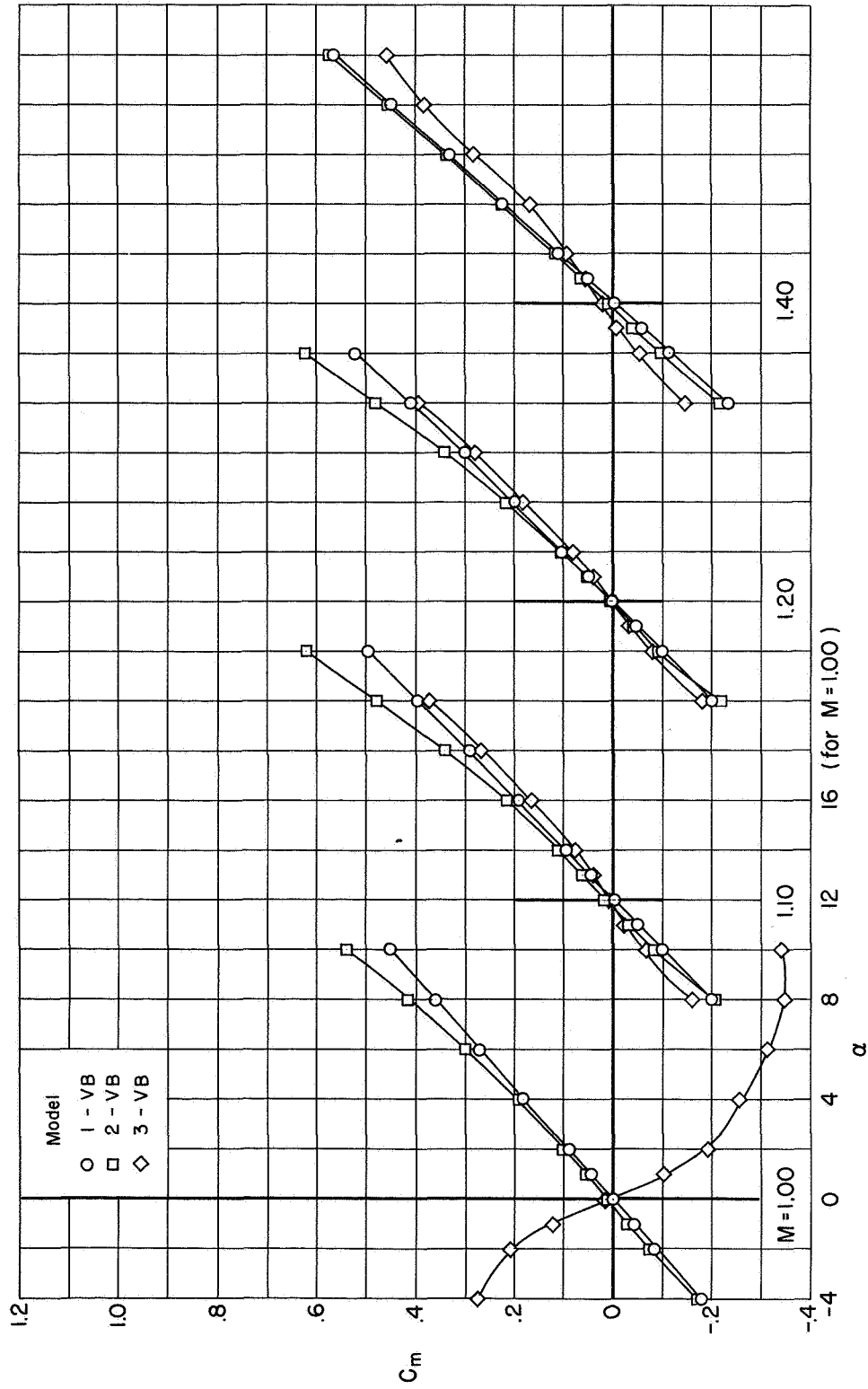
(b) $M = 1.00$ to 1.40

Figure 4.- Concluded.



(a) $M = 0.60$ to 0.90

Figure 5.- Effect of vehicle nose-shape on the variation of pitching-moment coefficient for vehicle models in the presence of a simulated booster rocket.



(b) $M = 1.00$ to 1.40

Figure 5.- Concluded.

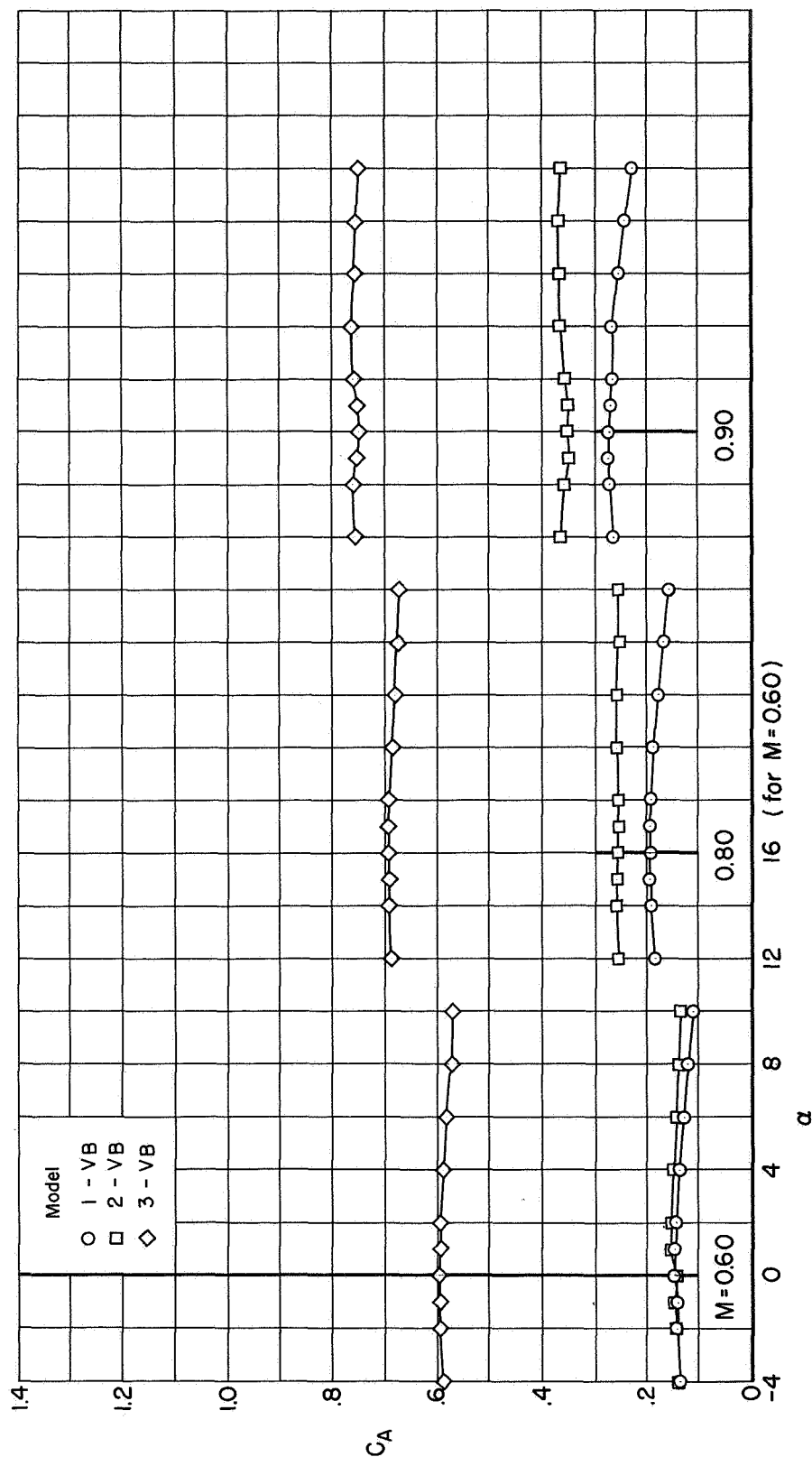
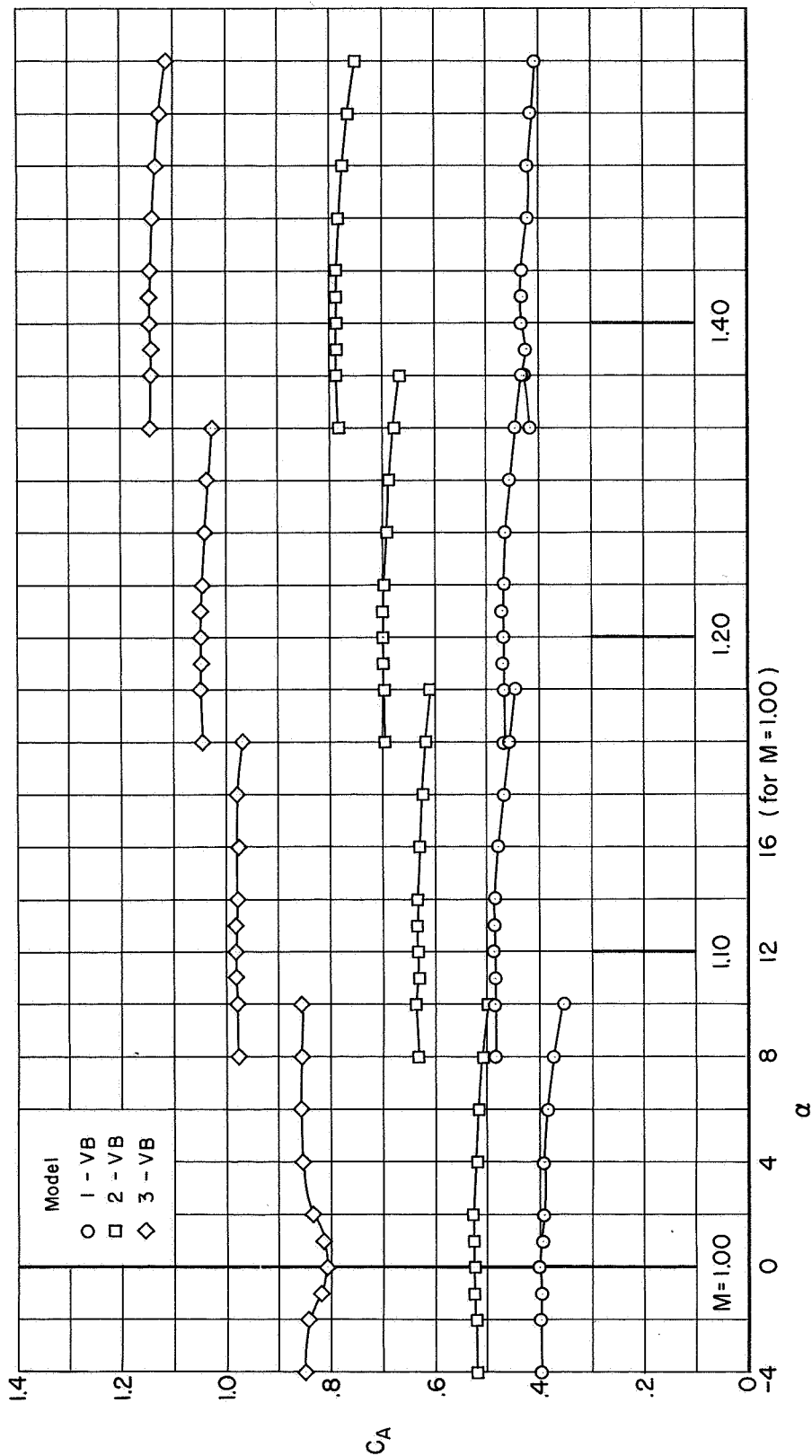
(a) $M = 0.60$ to 0.90

Figure 6.- Effect of vehicle nose-shape on the variation of axial-force coefficient for vehicle models in the presence of a simulated booster rocket.



(b) $M = 1.00$ to 1.40

Figure 6.- Concluded.

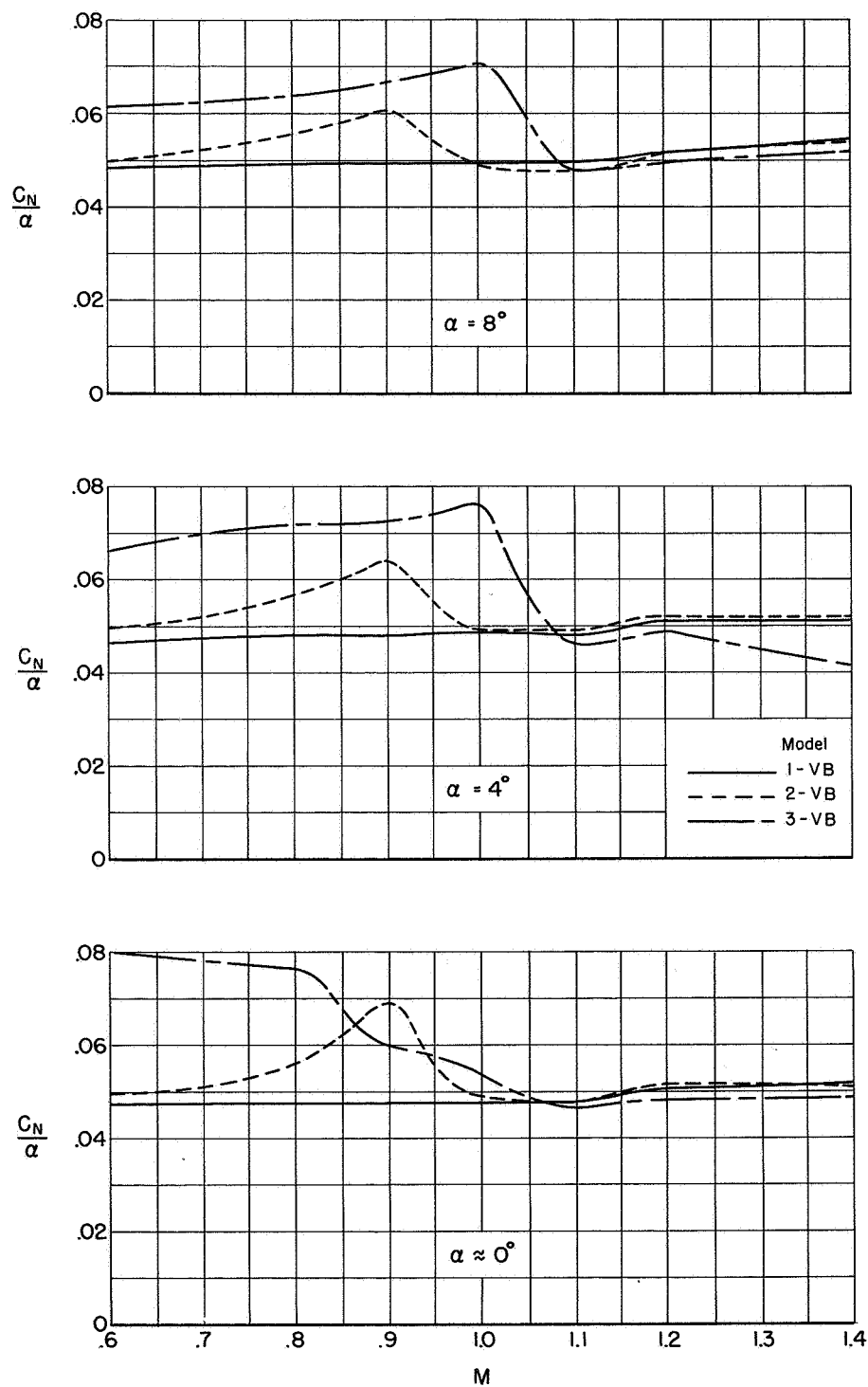


Figure 7.- Effect of vehicle nose-shape on the variation of normal-force parameter at selected angles of attack for vehicle models in the presence of a simulated booster rocket.

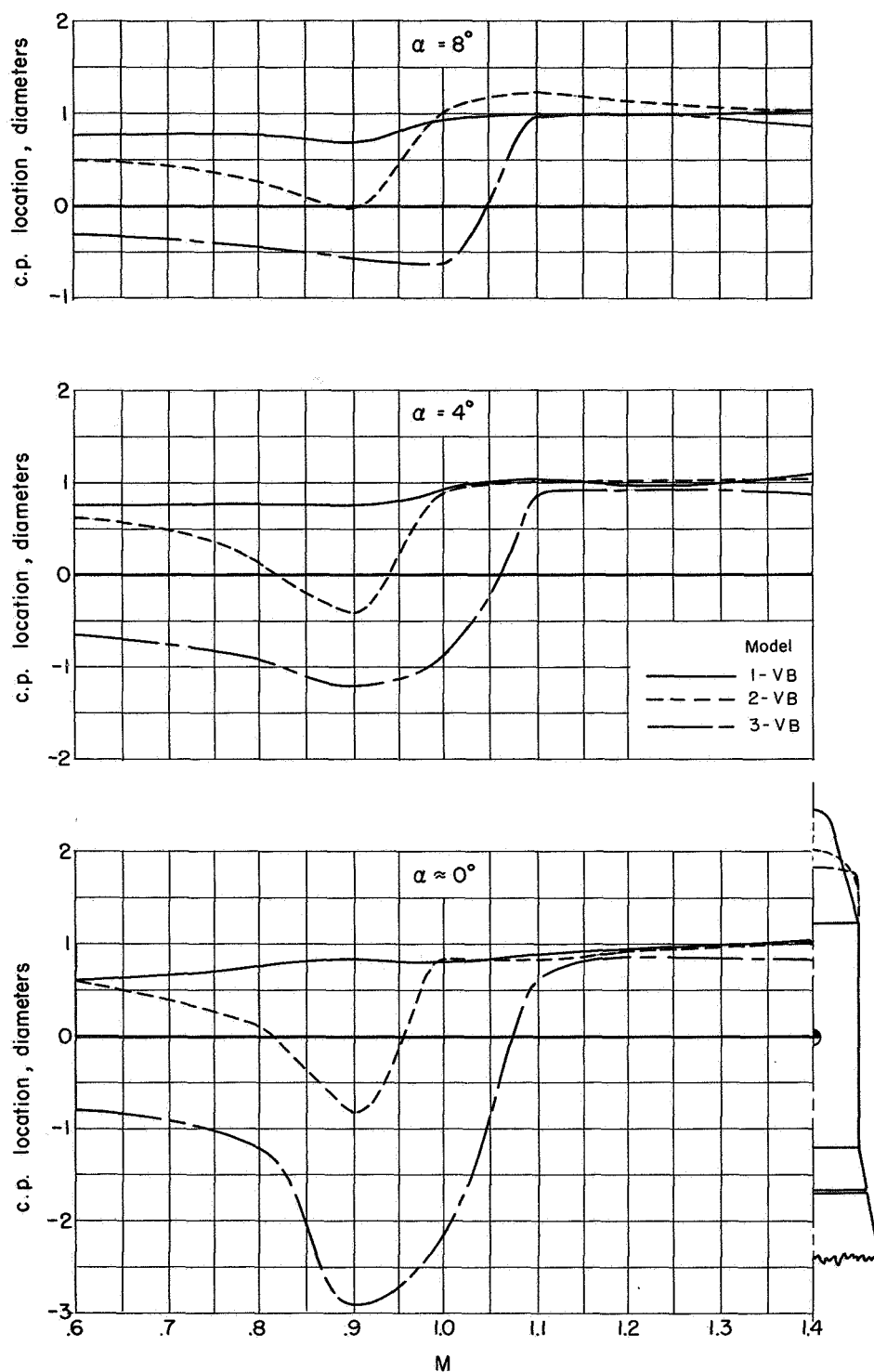


Figure 8.- Effect of vehicle nose-shape on the variation of center of pressure at selected angles of attack for vehicle models in the presence of a simulated booster rocket.

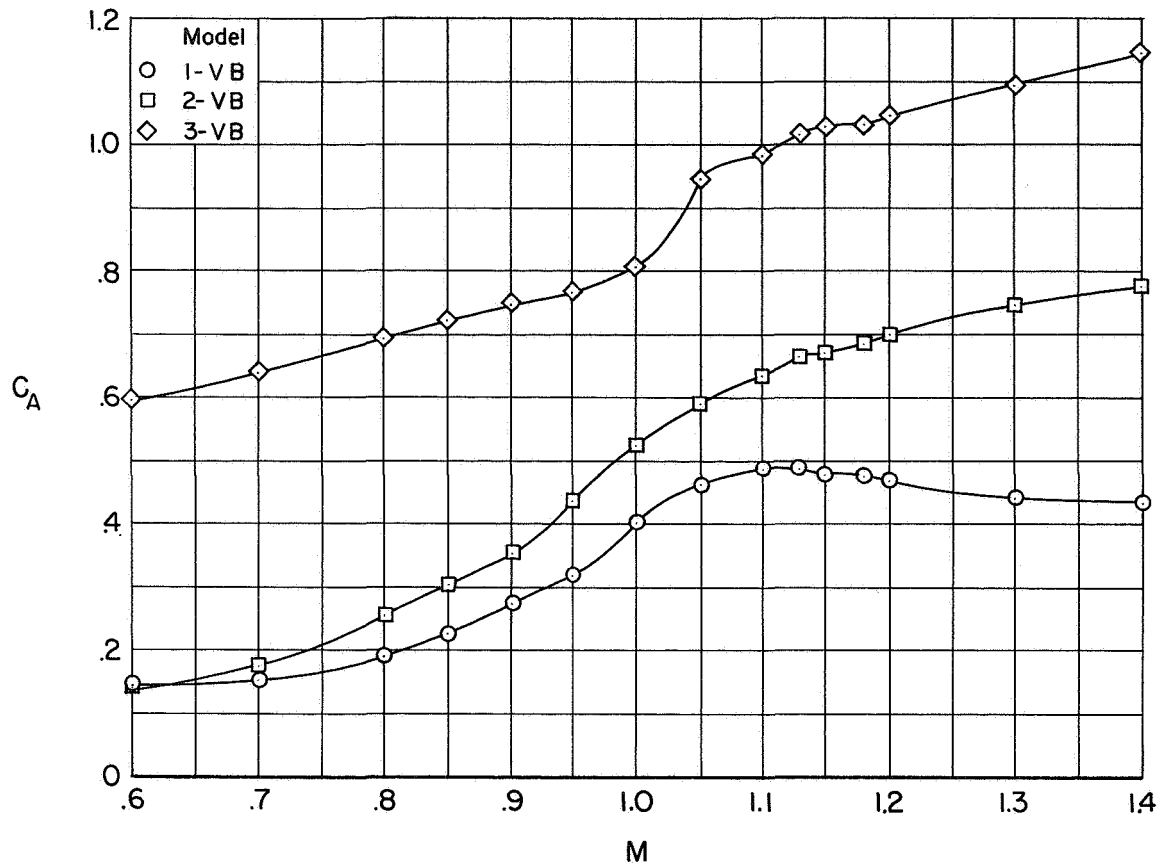
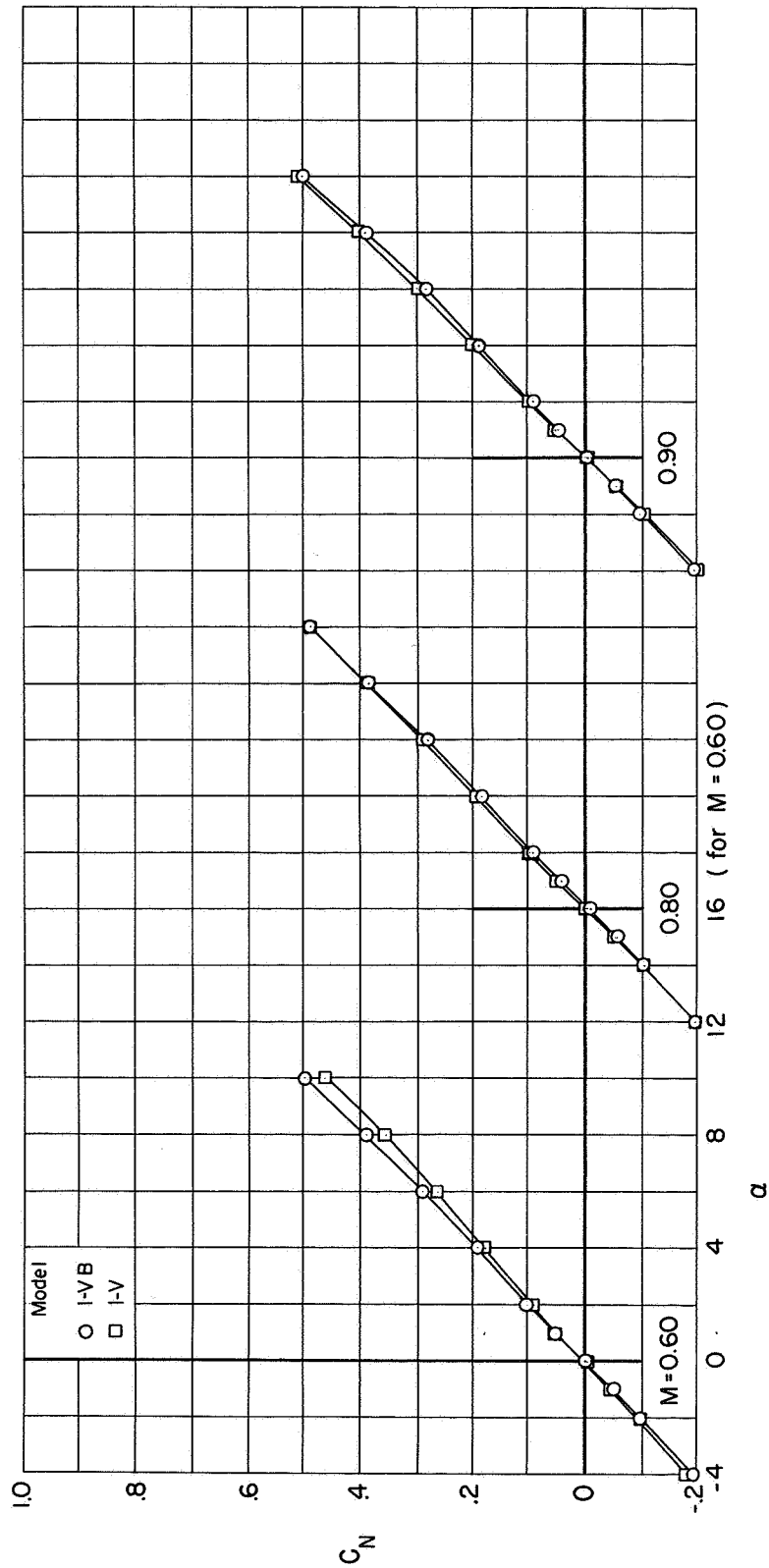
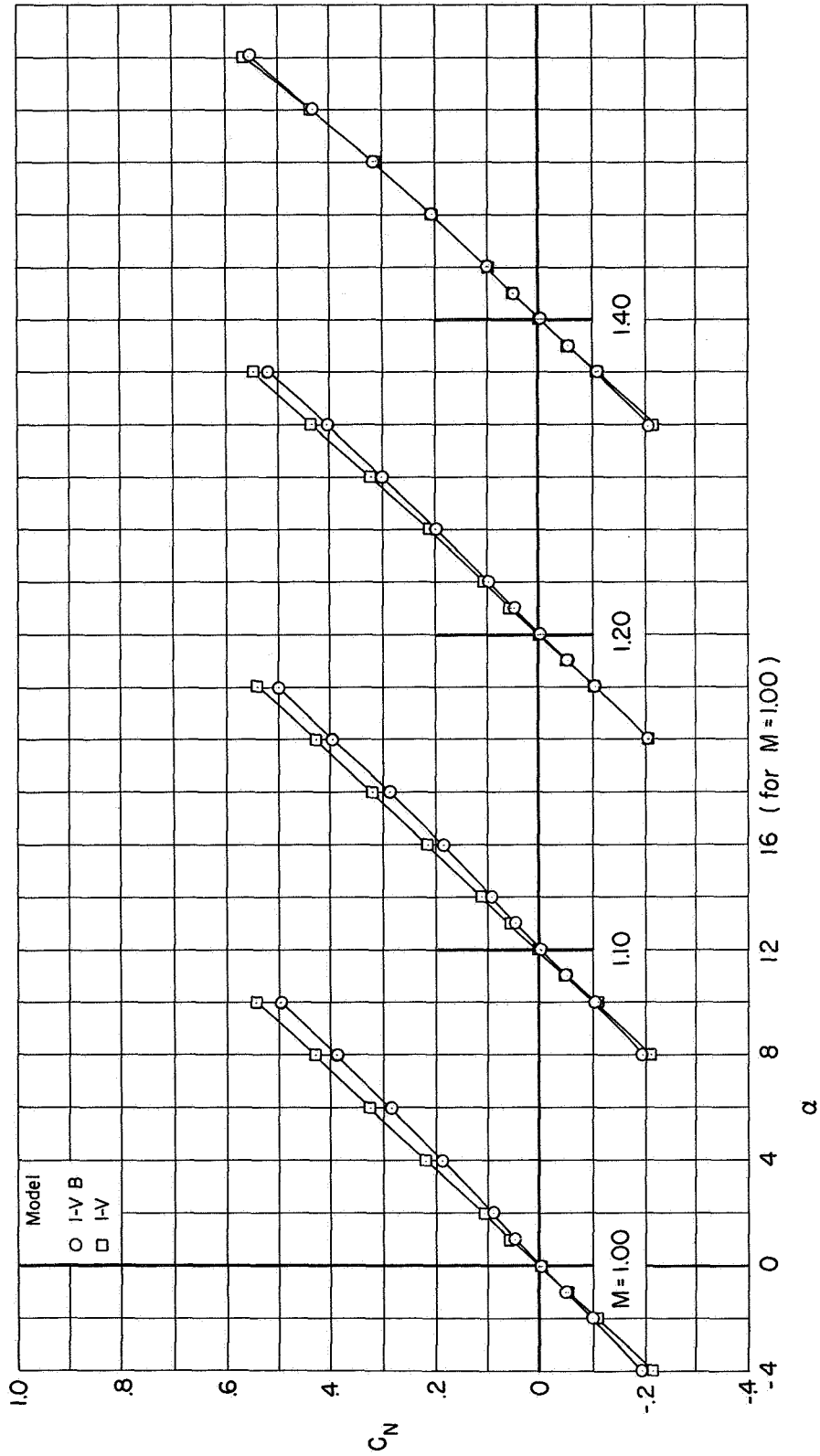


Figure 9.- Effect of vehicle nose-shape on the variation of axial-force coefficient at zero angle of attack for vehicle models in the presence of a simulated booster rocket.



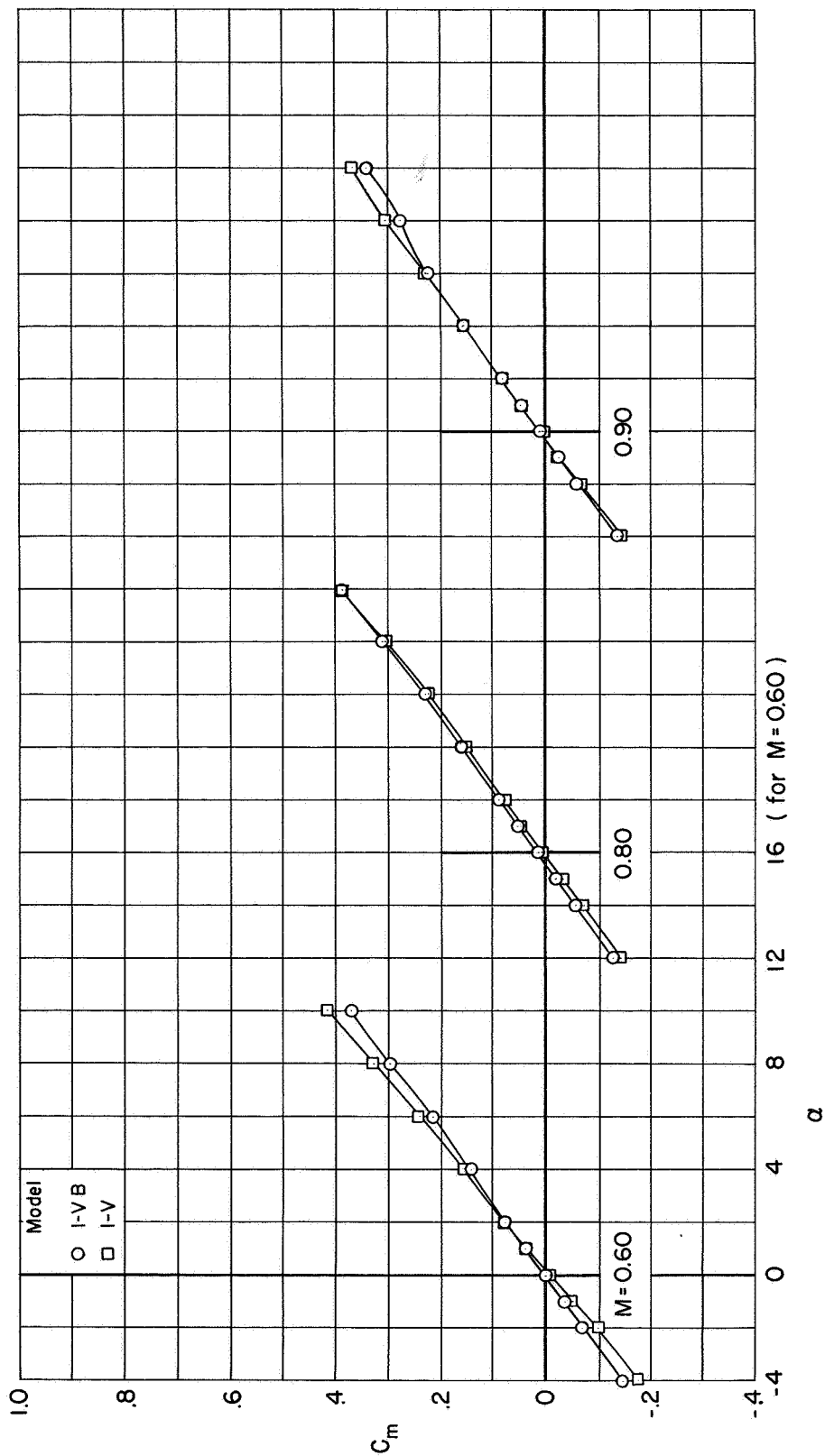
(a) $M = 0.60$ to 0.90

Figure 10.- Effect of the presence of a simulated booster rocket on the variation of normal-force coefficient for a vehicle model.



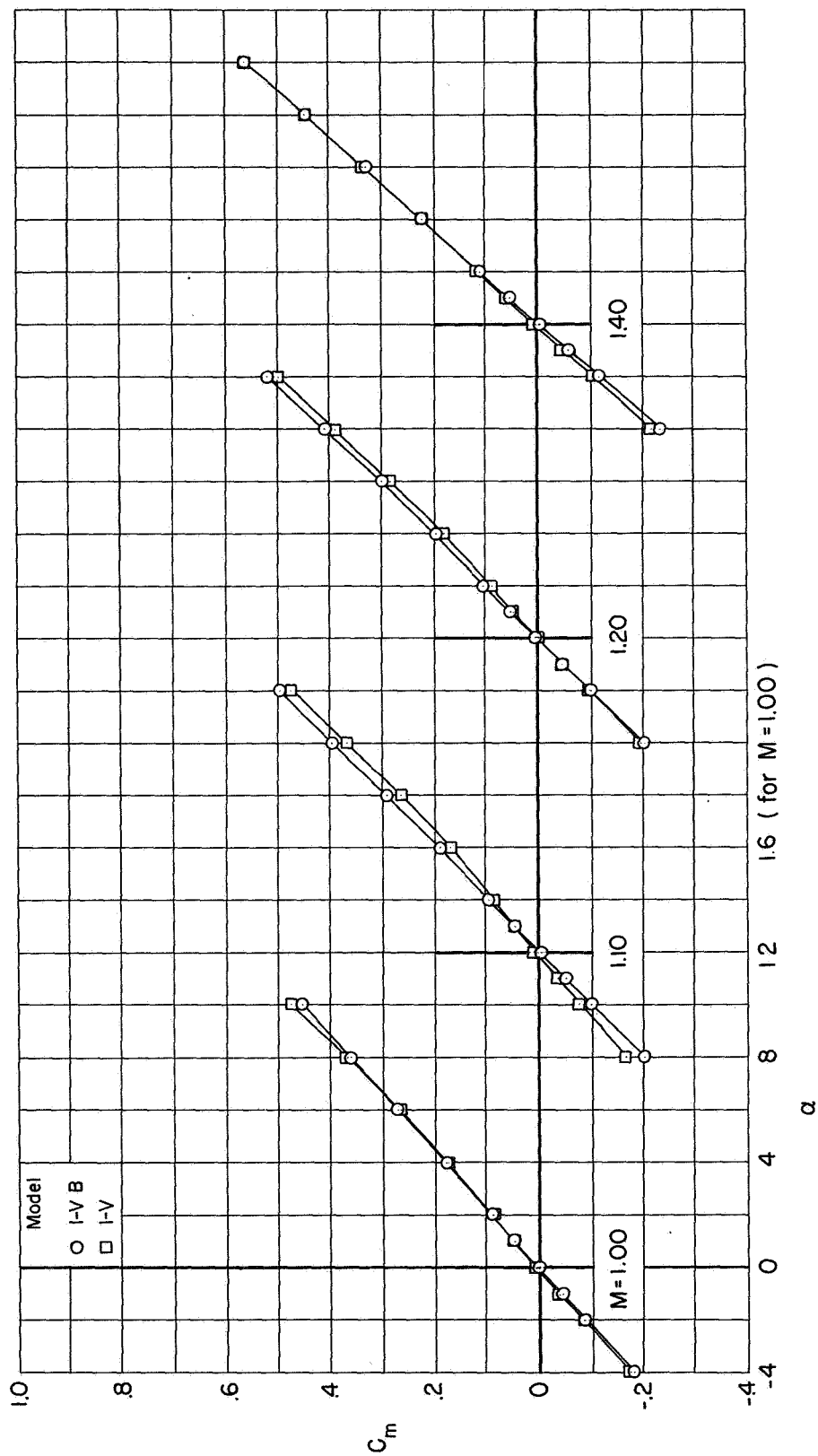
(b) $M = 1.00$ to 1.40 .

Figure 10.- Concluded.



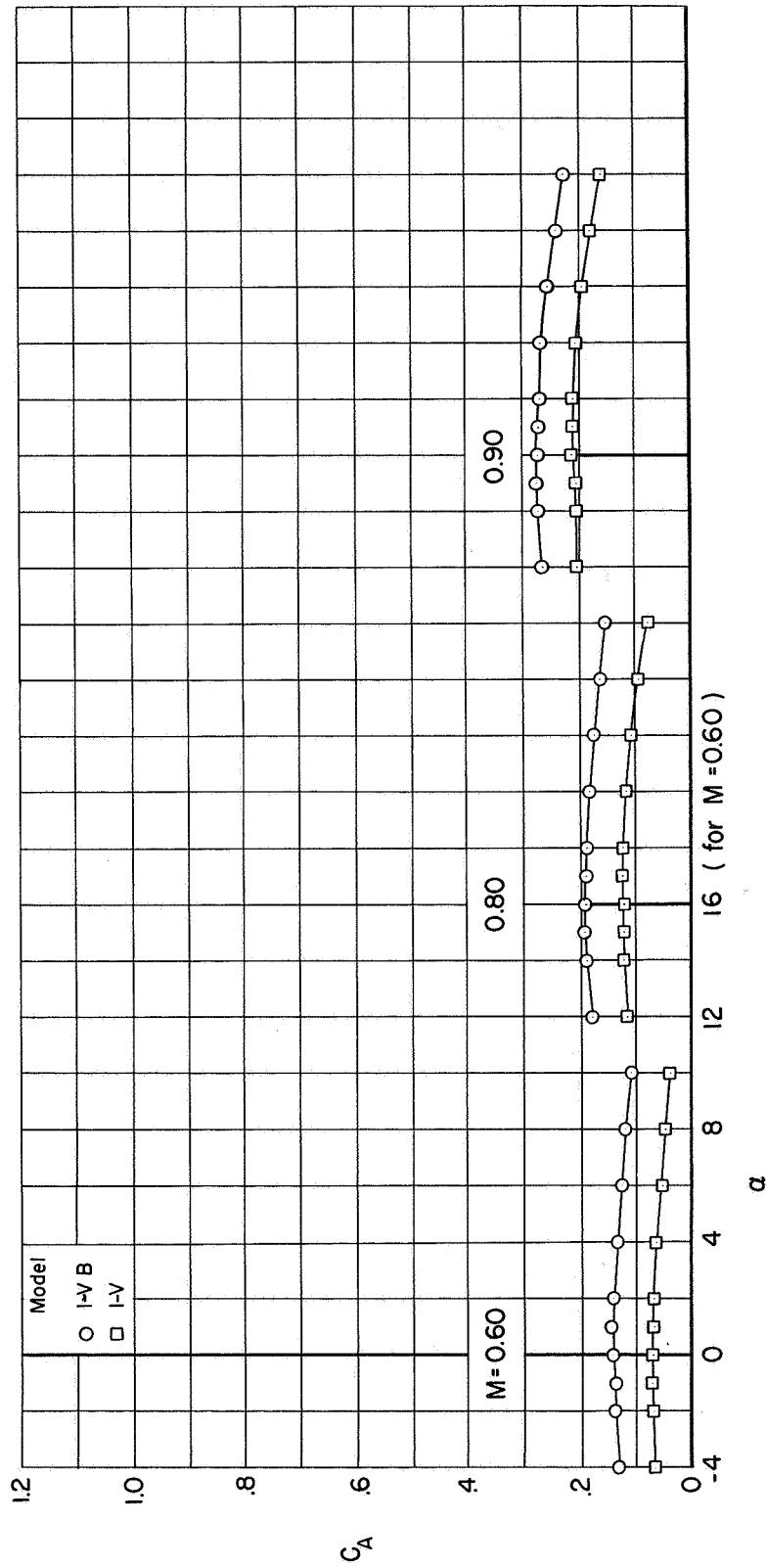
(a) $M = 0.60$ to 0.90

Figure 11.- Effect of the presence of a simulated booster rocket on the variation of pitching-moment coefficient for a vehicle model.



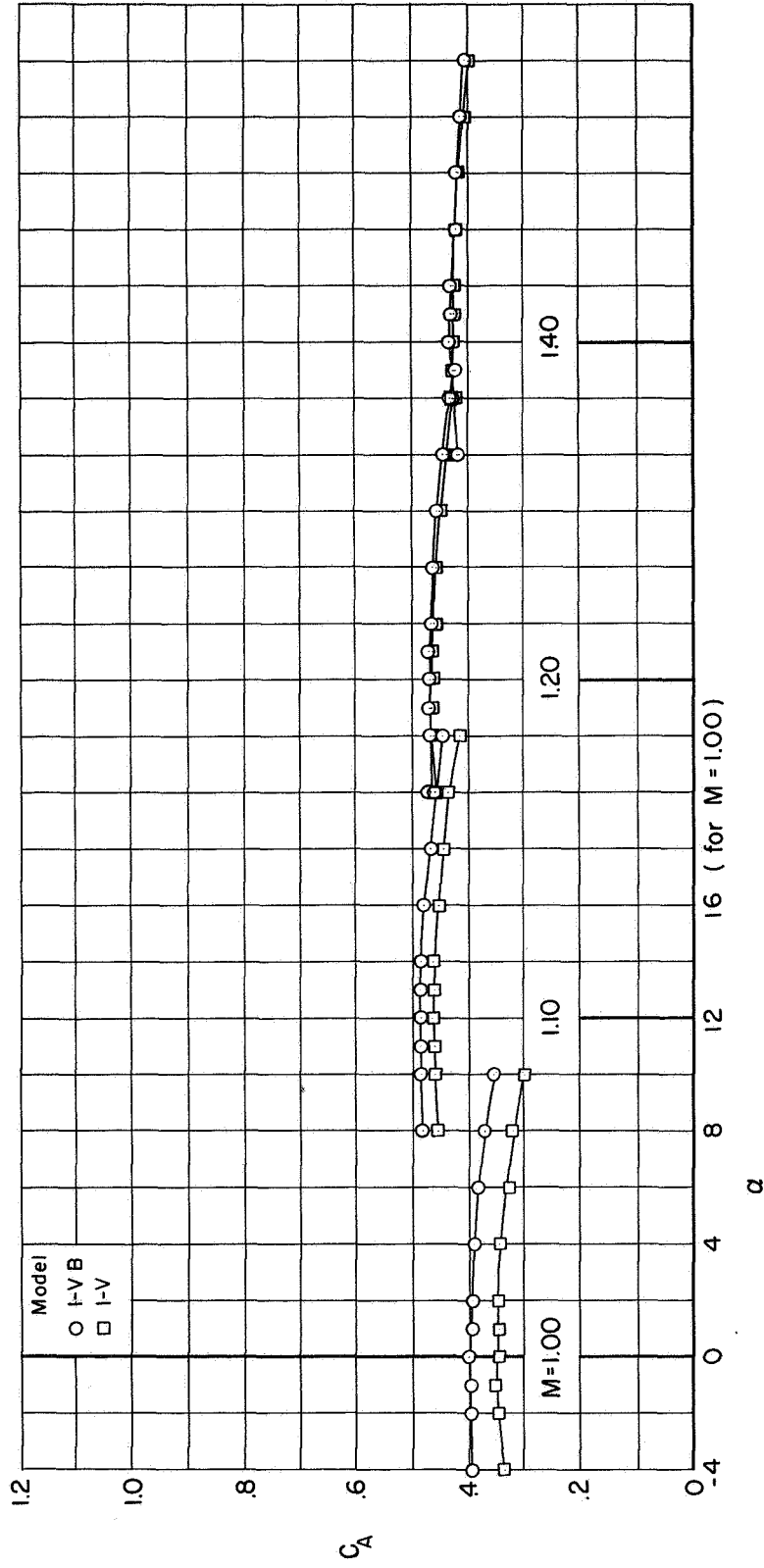
(b) $M = 1.00$ to 1.40 .

Figure 11.- Concluded.



(a) $M = 0.60$ to 0.90

Figure 12.- Effect of the presence of a simulated booster rocket on the variation of axial-force coefficient for a vehicle model.



(b) $M = 1.00$ to 1.40

Figure 12.- Concluded.

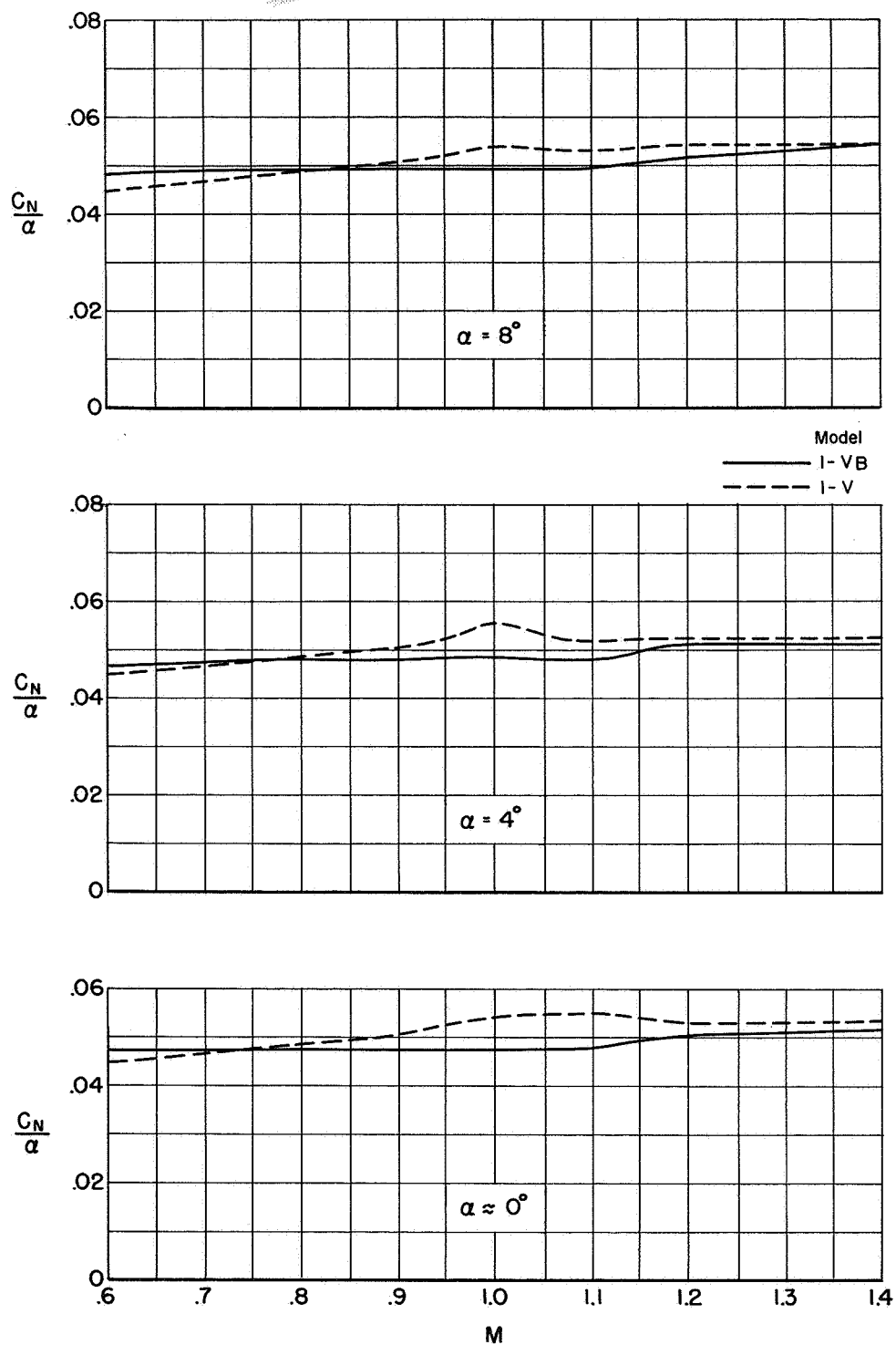


Figure 13.- Effect of the presence of a simulated booster rocket on the variation of normal-force parameter at selected angles of attack for a vehicle model.

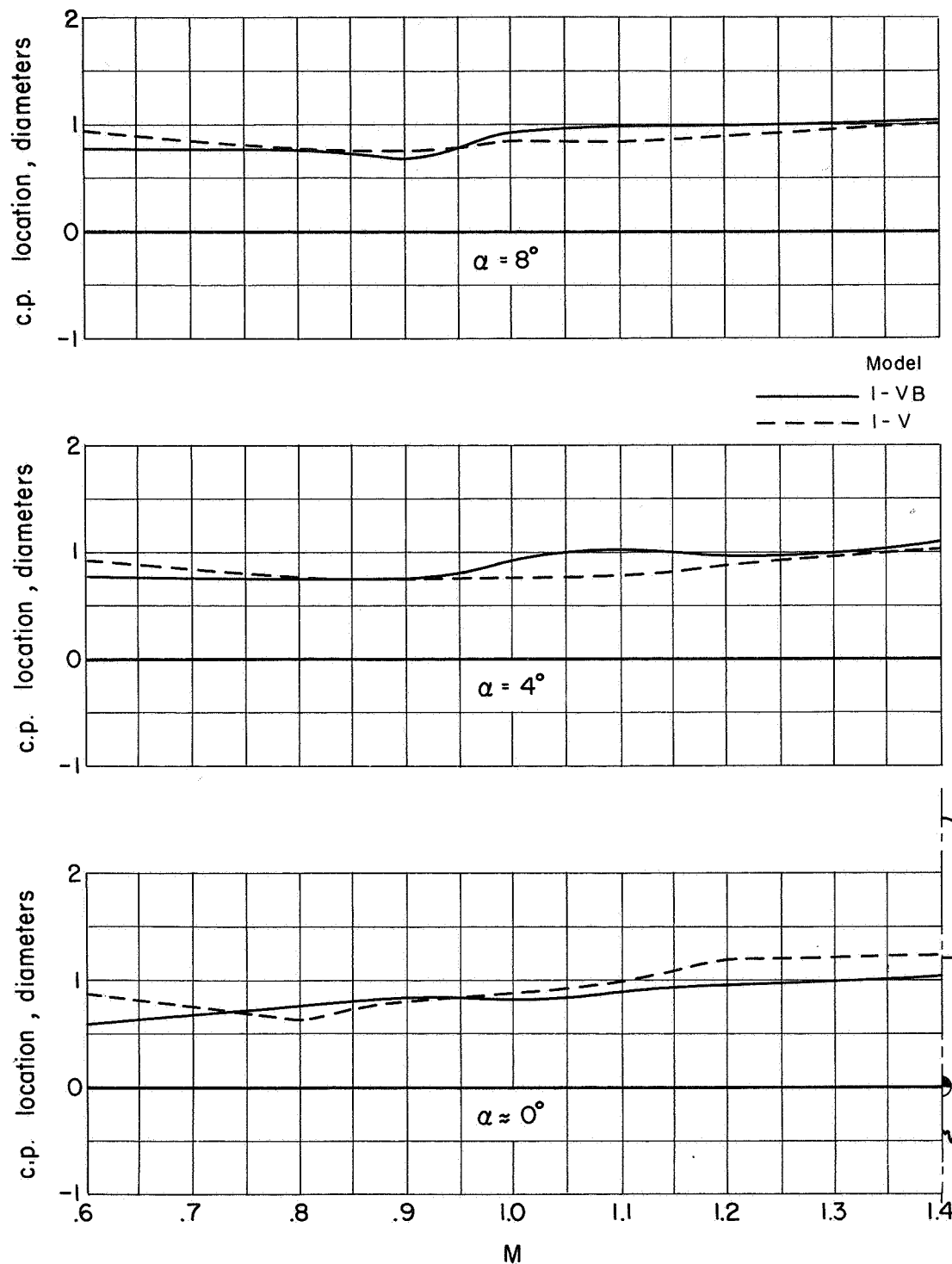


Figure 14.- Effect of the presence of a simulated booster rocket on the variation of center of pressure at selected angles of attack for a vehicle model.

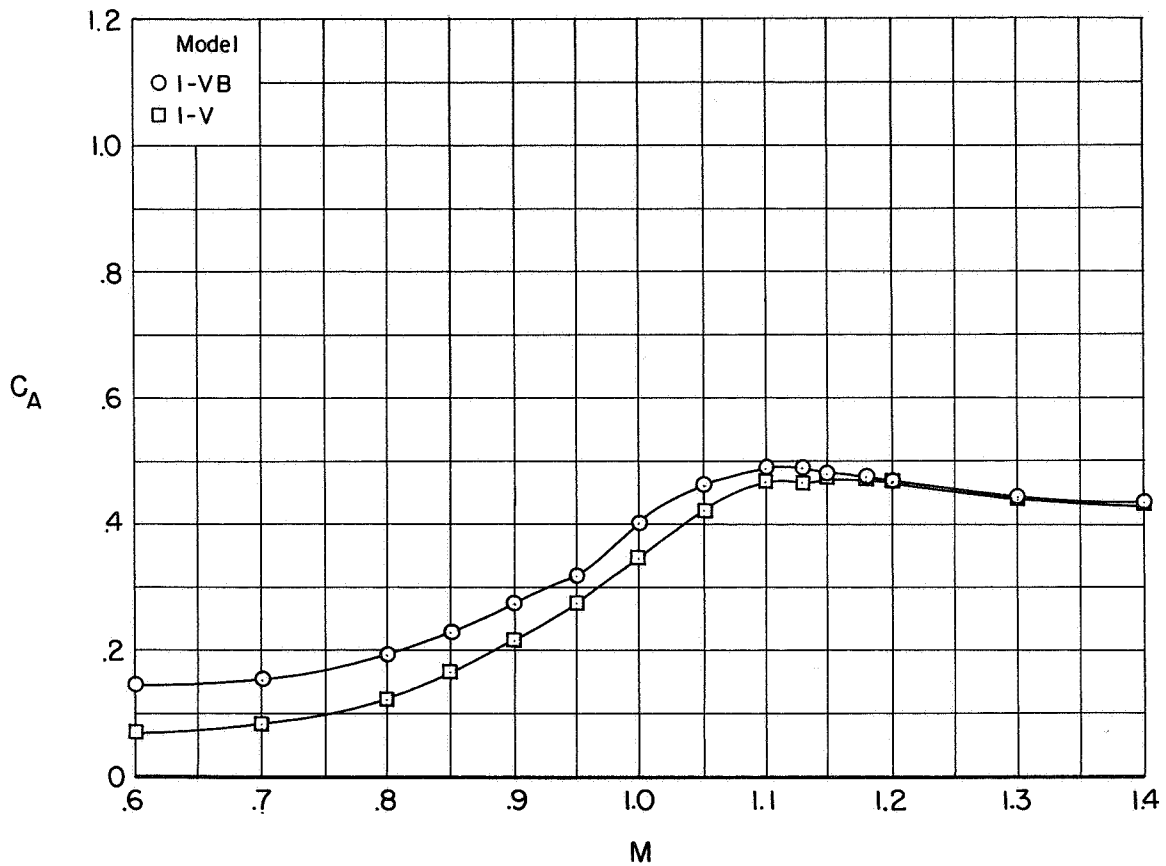


Figure 15.- Effect of the presence of a simulated booster rocket on the variation of axial-force coefficient at zero angle of attack for a vehicle model.

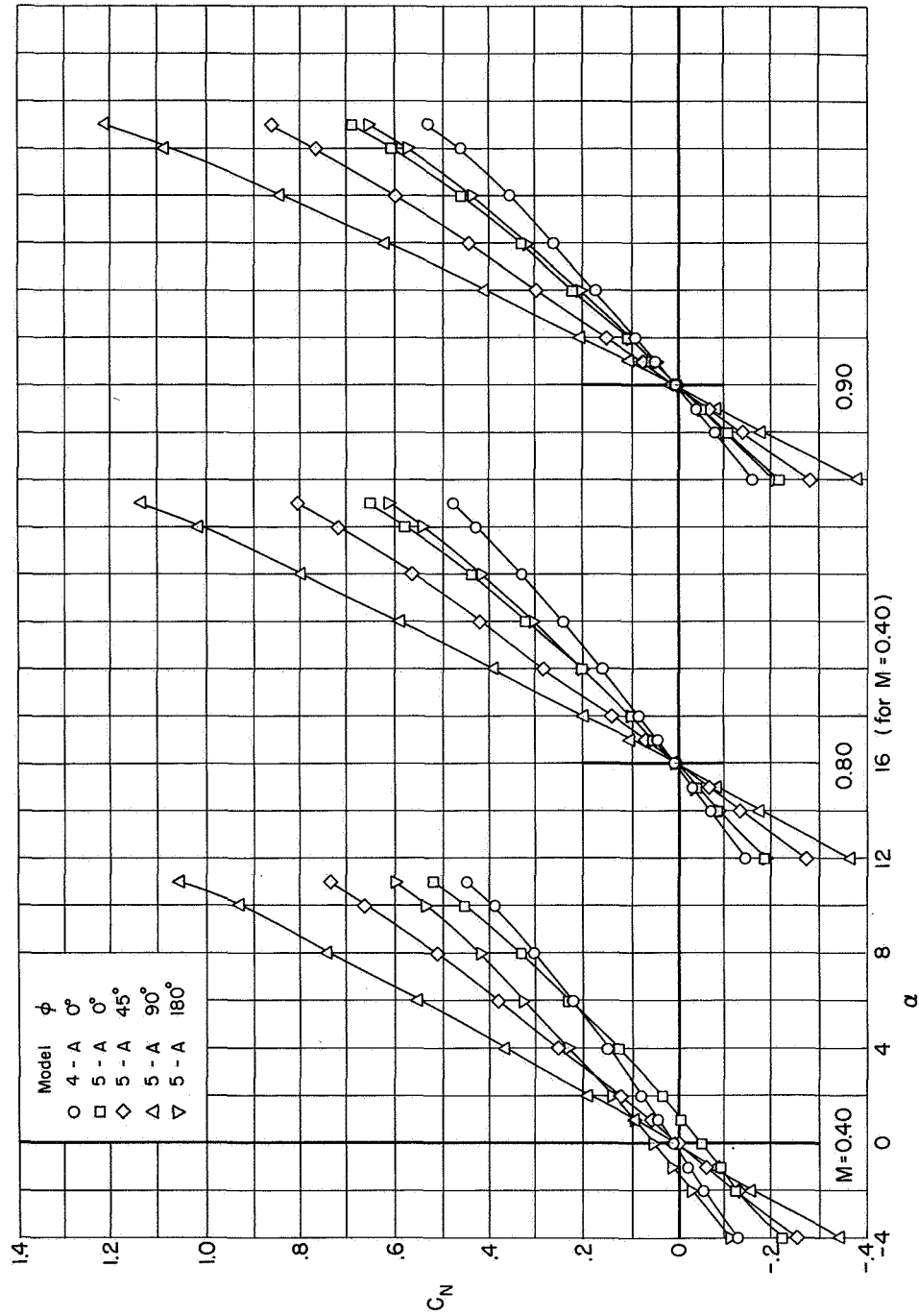
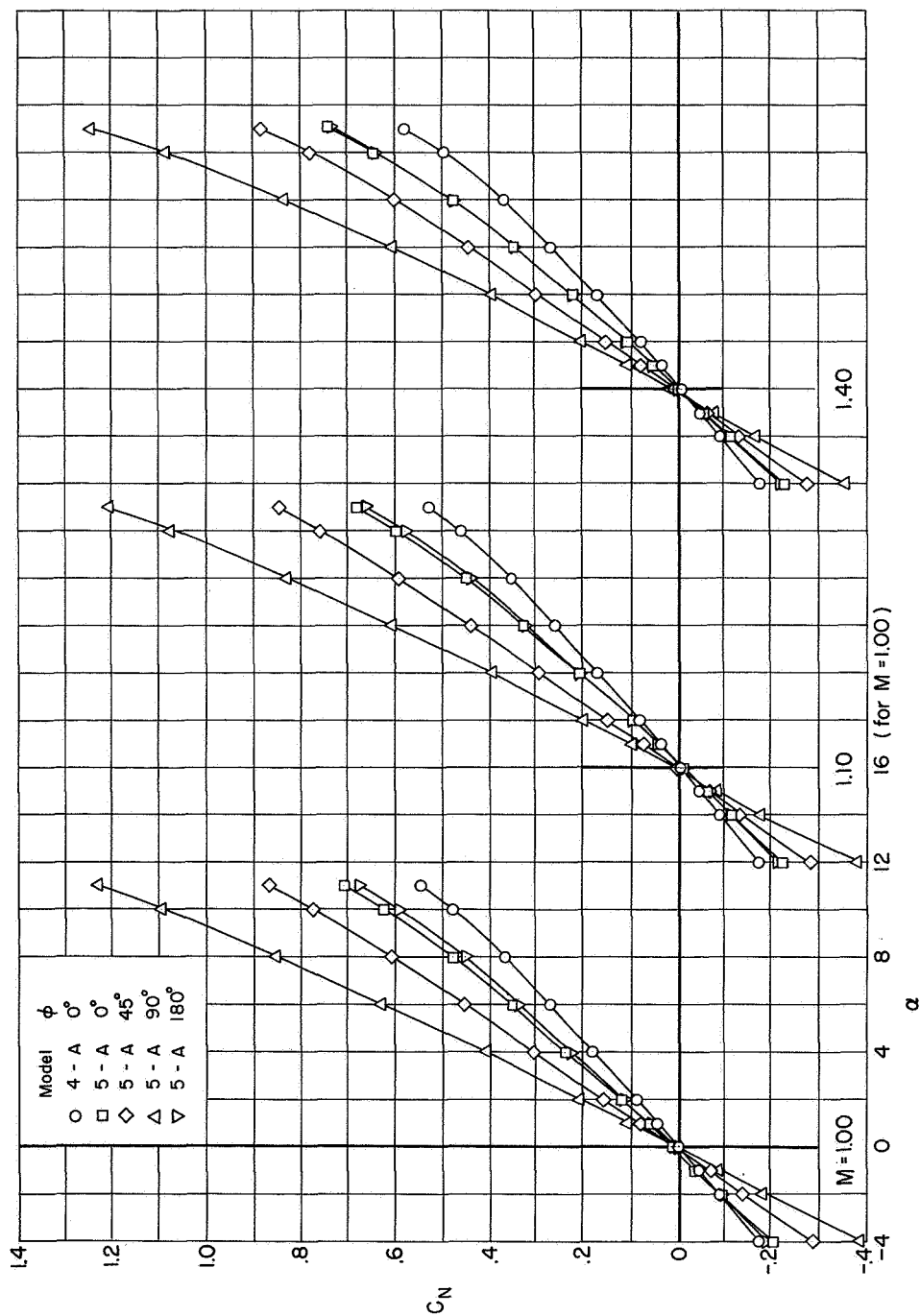
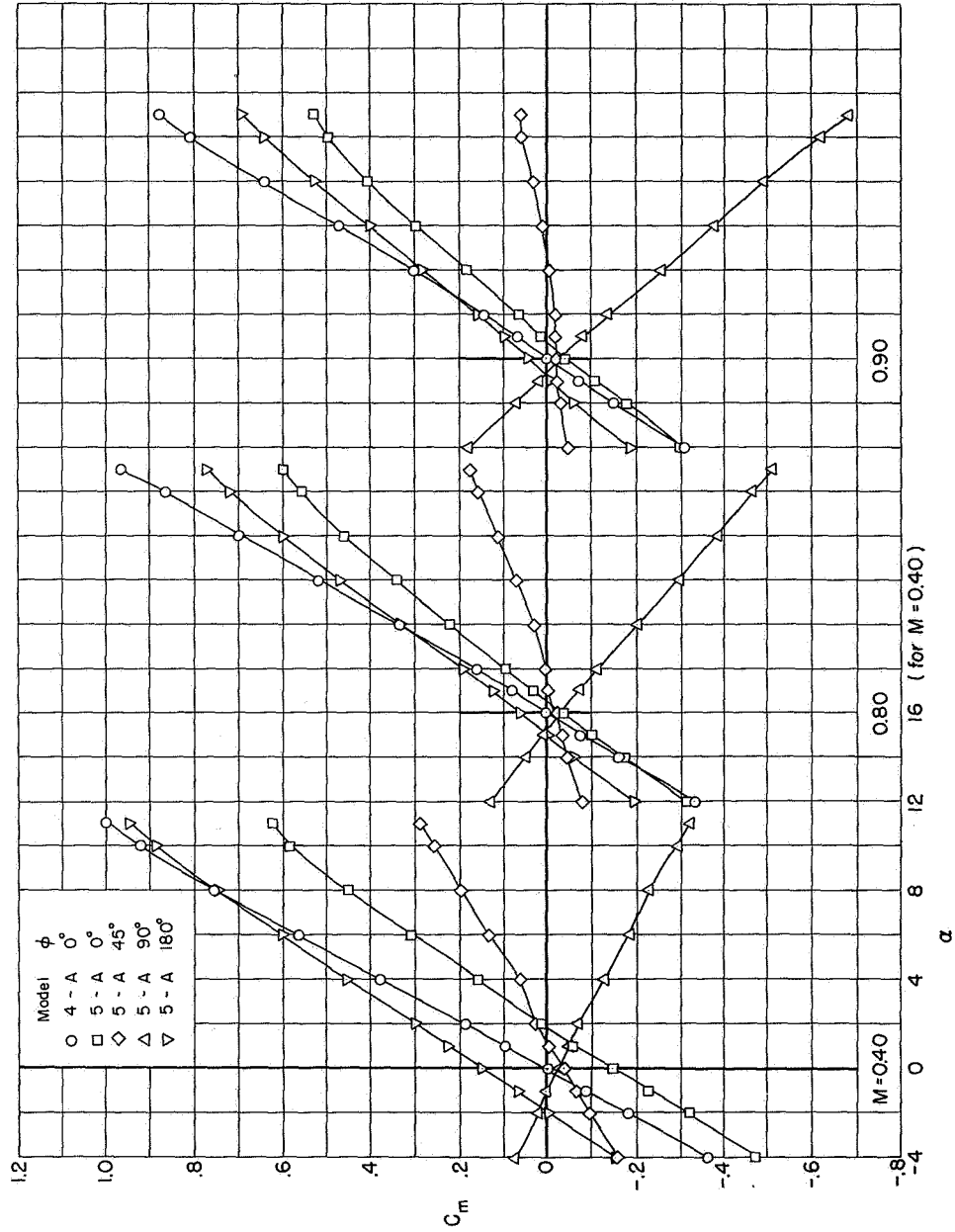
(a.) $M = 0.40$ to 0.90

Figure 16.- Effect of asymmetric protuberances and model roll angle on the variation of normal force coefficient for rocket assembly models.



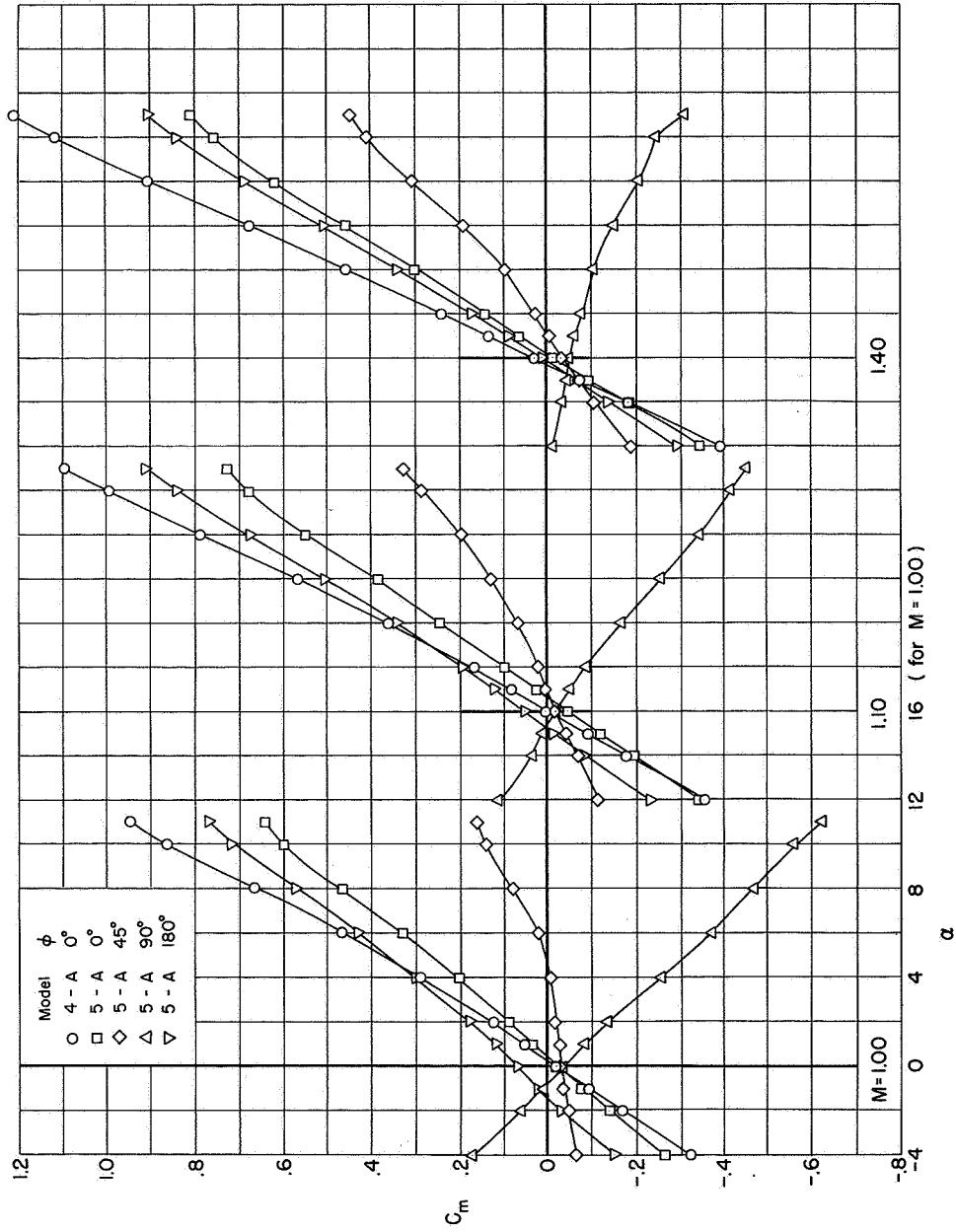
(b) $M = 1.00$ to 1.40 .

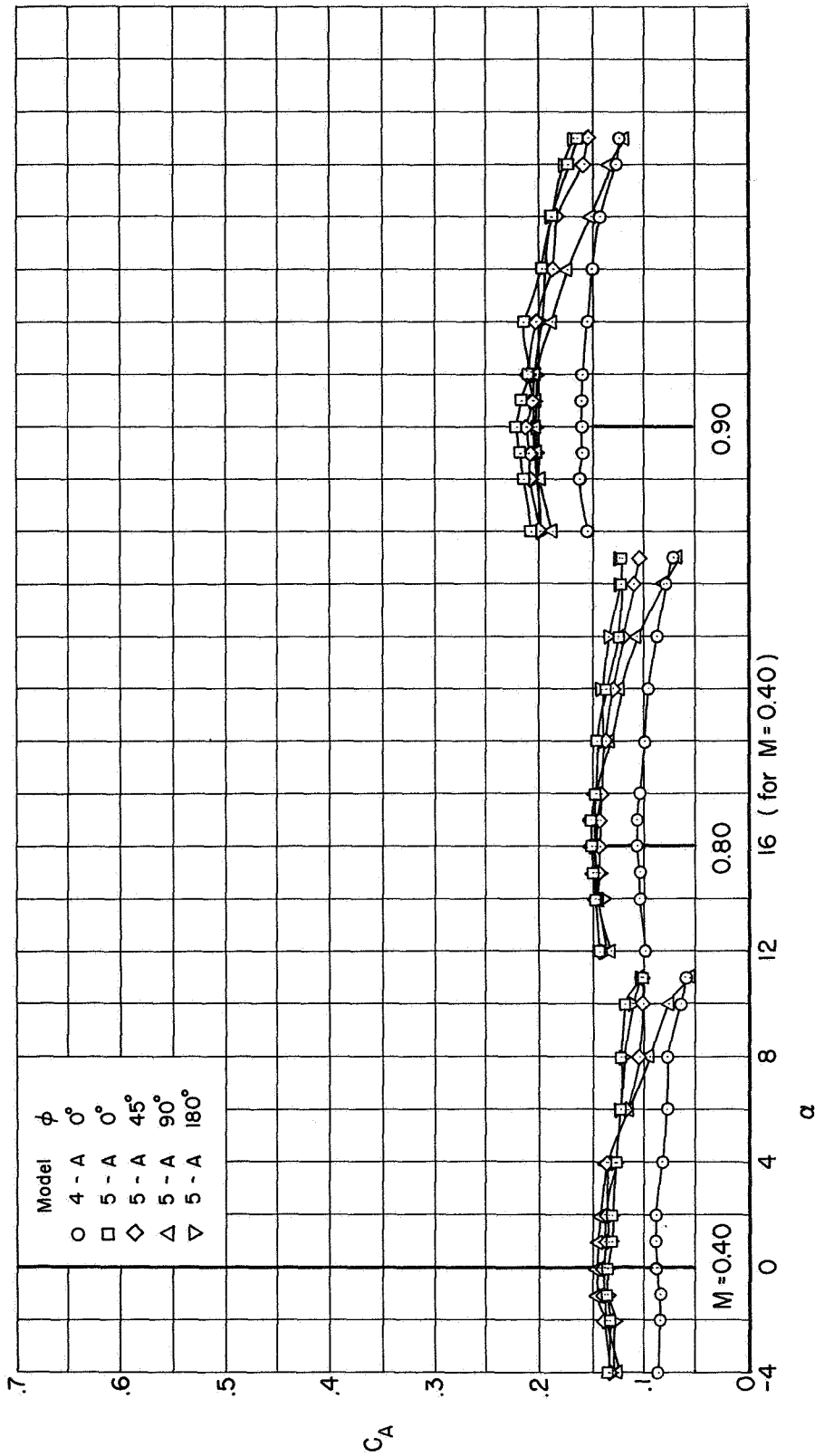
Figure 16.- Concluded.



(a) $M = 0.40$ to 0.90

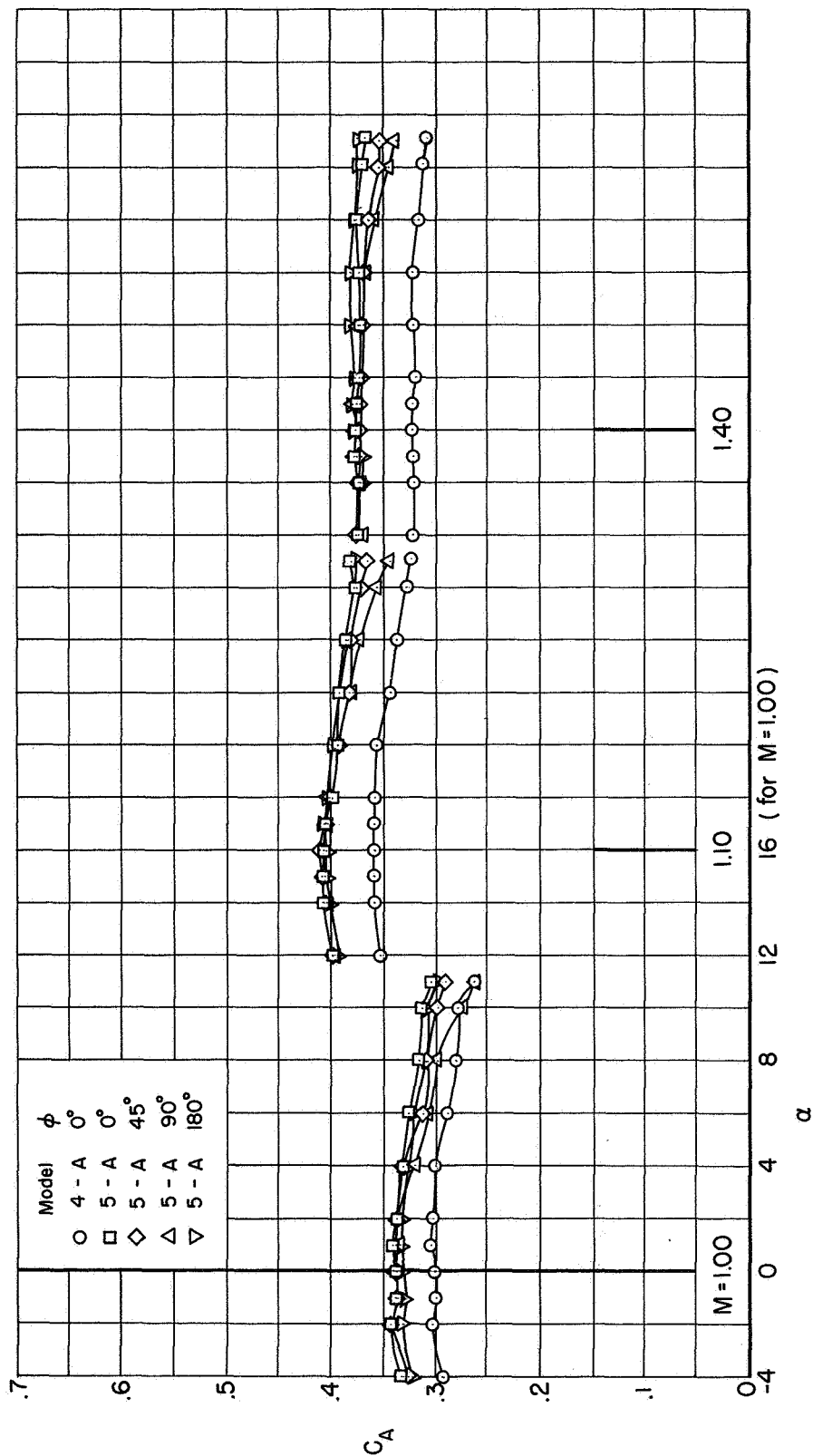
Figure 17.- Effect of asymmetric protuberances and model roll angle on the variation of pitching-moment coefficient for rocket assembly models.



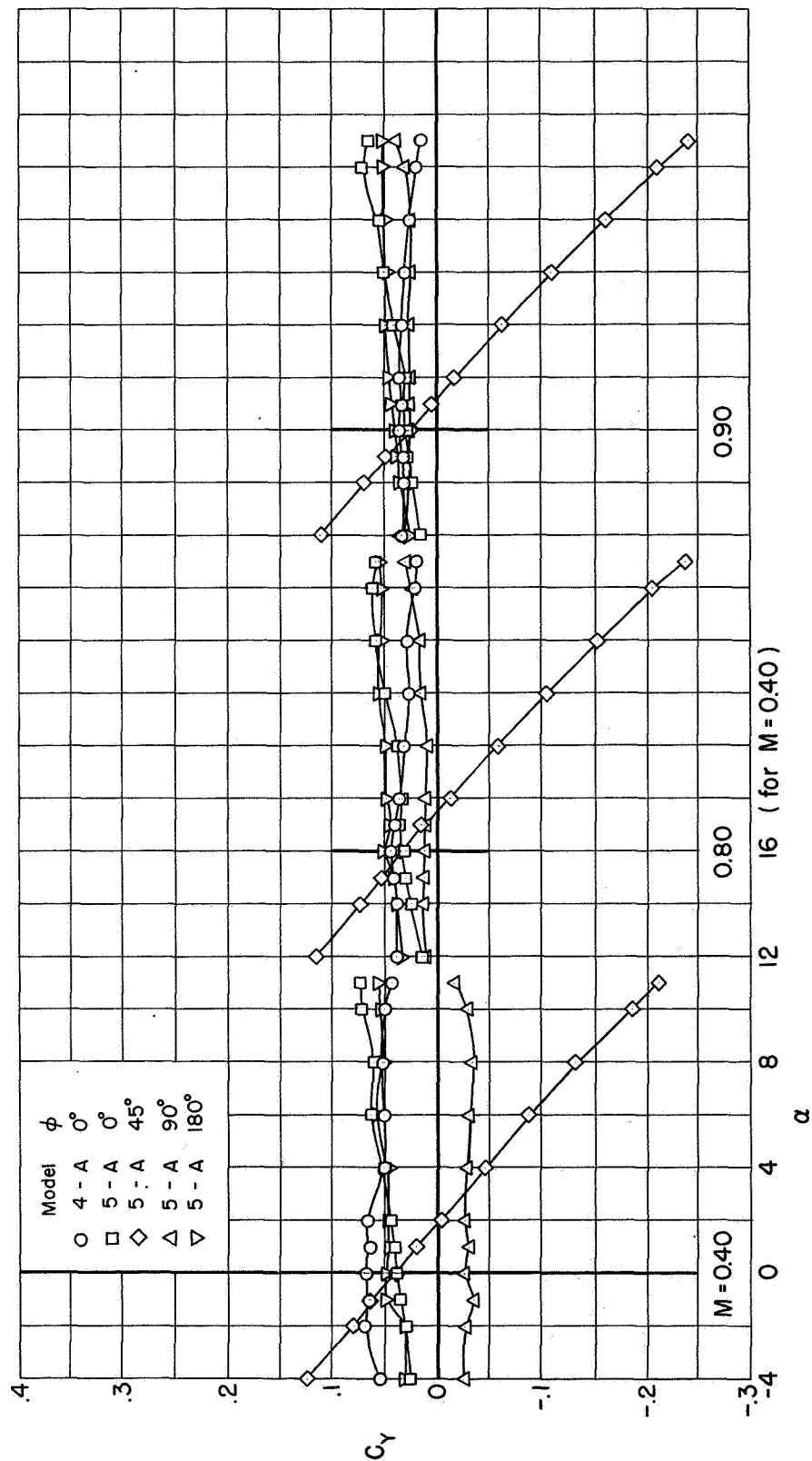


(a) $M = 0.40$ to 0.90

Figure 18.- Effect of asymmetric protuberances and model roll angle on the variation of axial force coefficient for rocket assembly models.

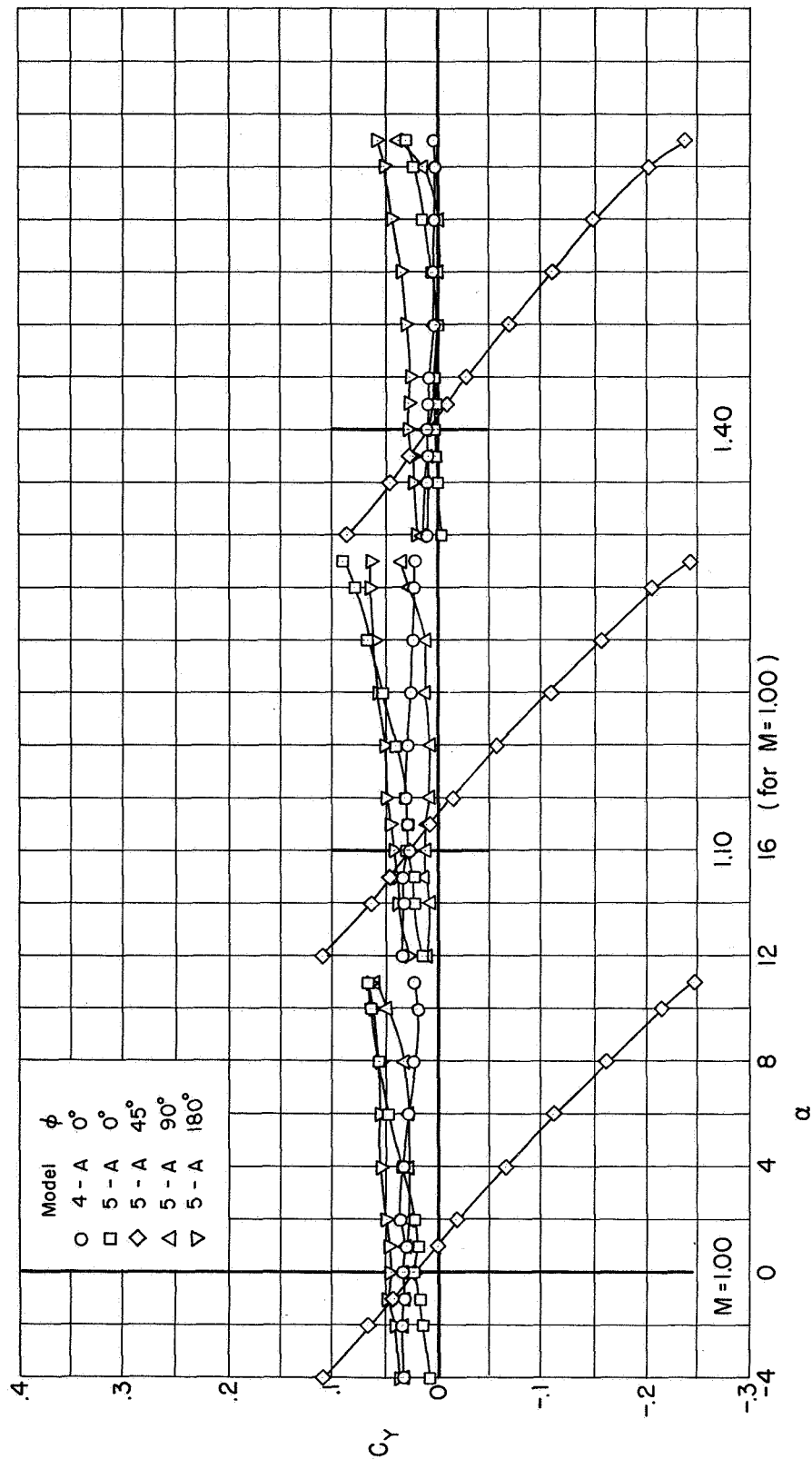


(b) $M = 1.00$ to 1.40
Figure 18.- Concluded.



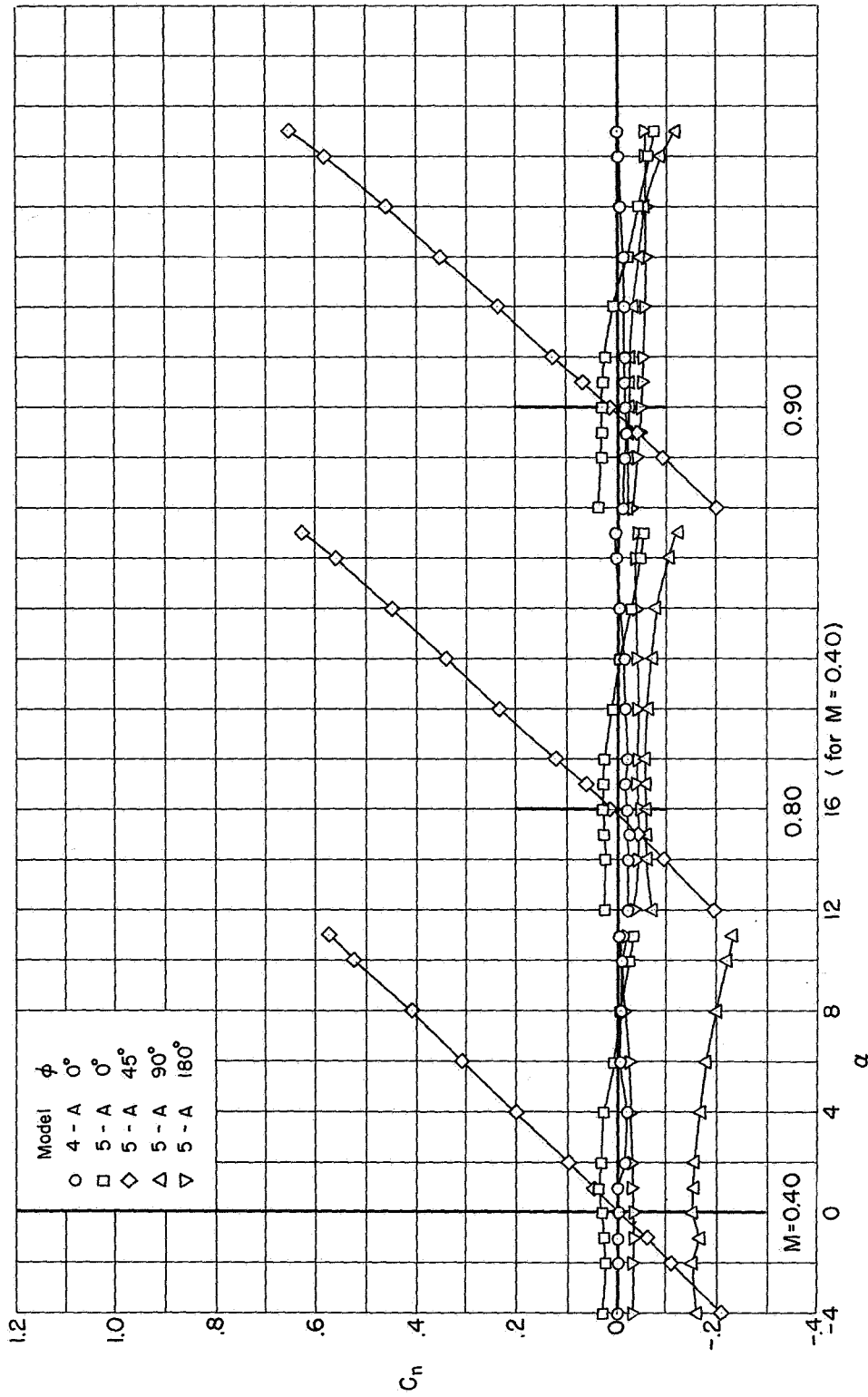
(a) $M = 0.40$ to 0.90

Figure 19.- Effect of asymmetric protuberances and model roll angle on the variation of side-force coefficient for rocket assembly models.



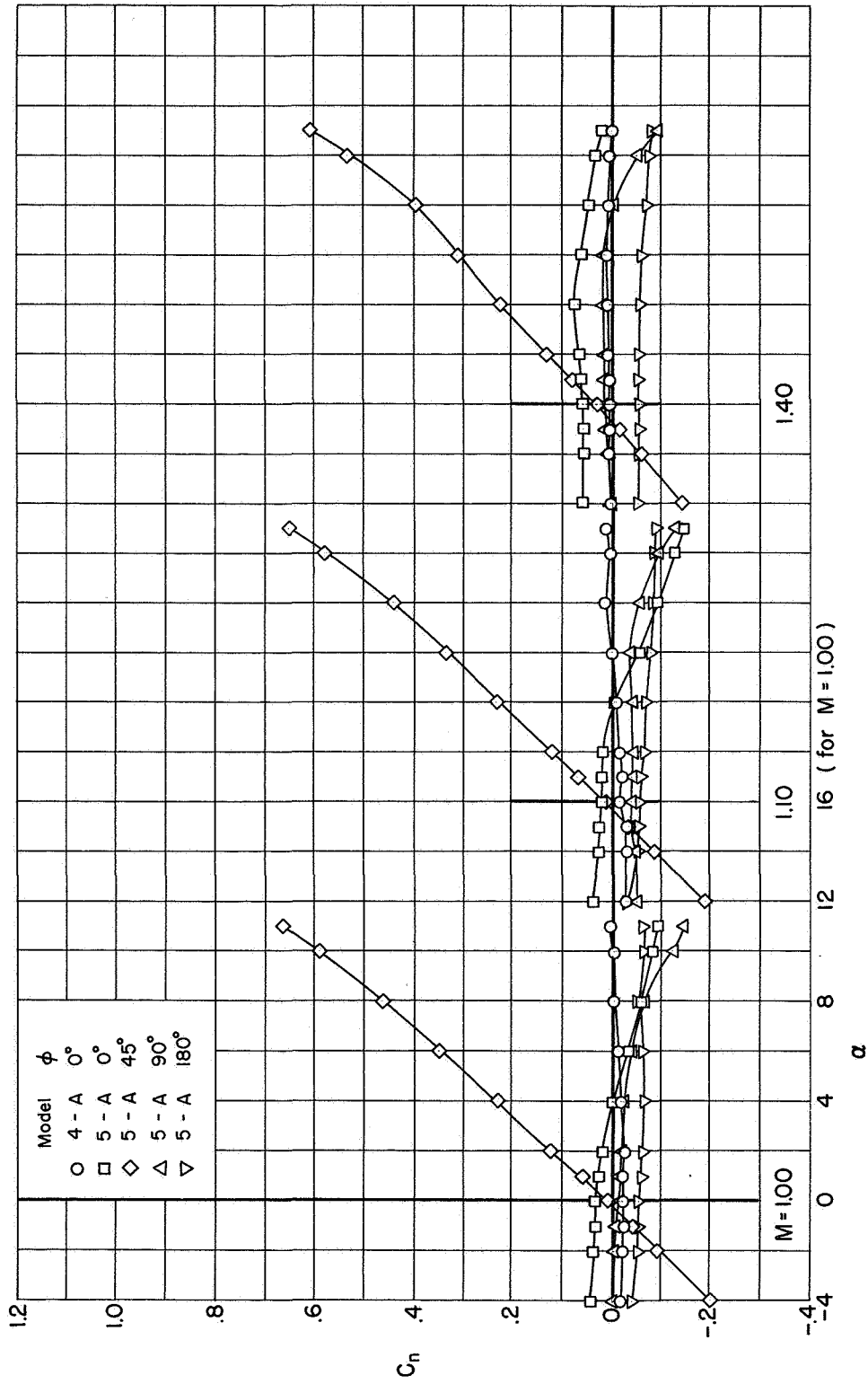
(b) $M = 1.00$ to 1.40

Figure 19.- Concluded.



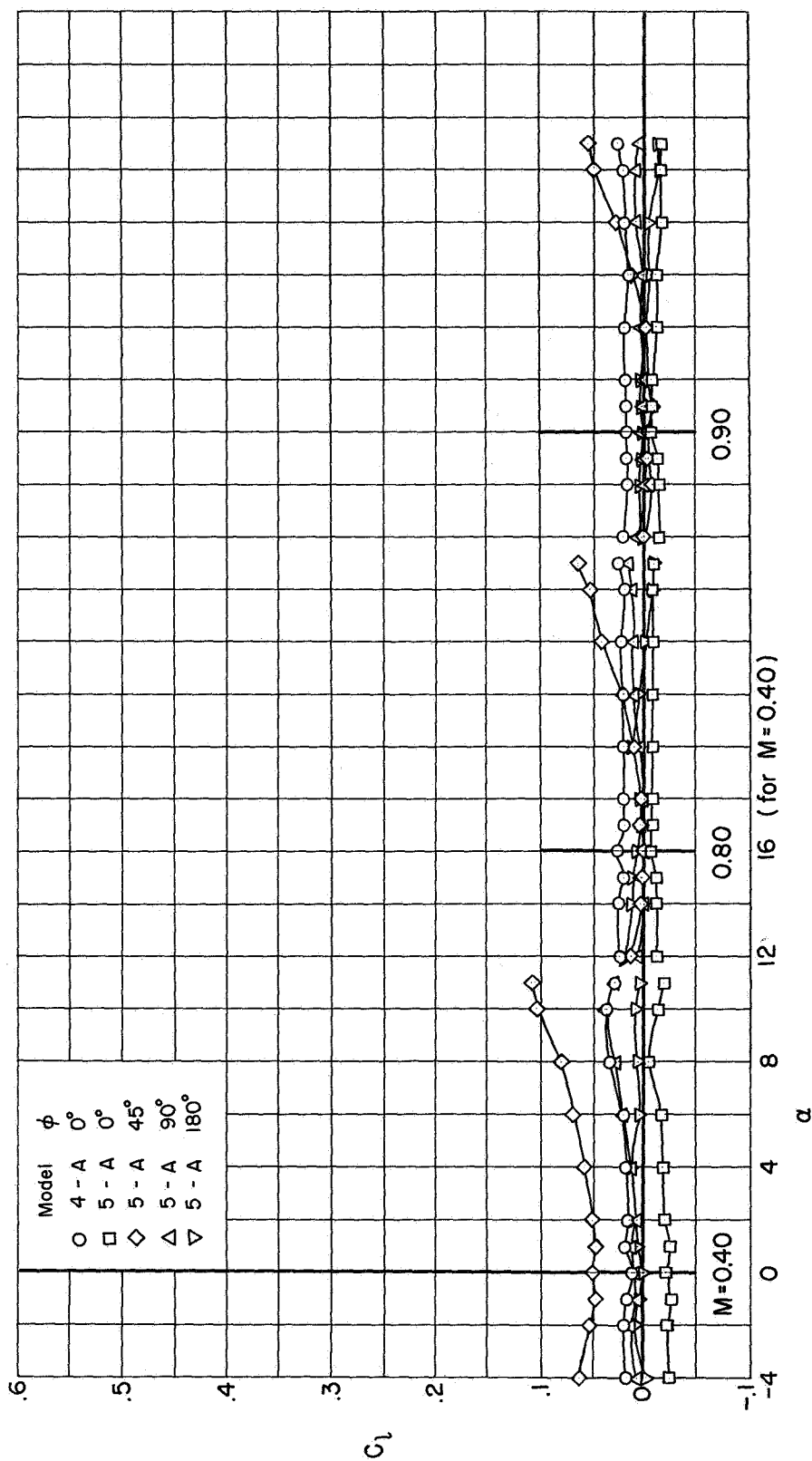
(a) $M = 0.40$ to 0.90

Figure 20.- Effect of asymmetric protuberances and model roll angle on the variation of yawing moment coefficient for rocket assembly models.



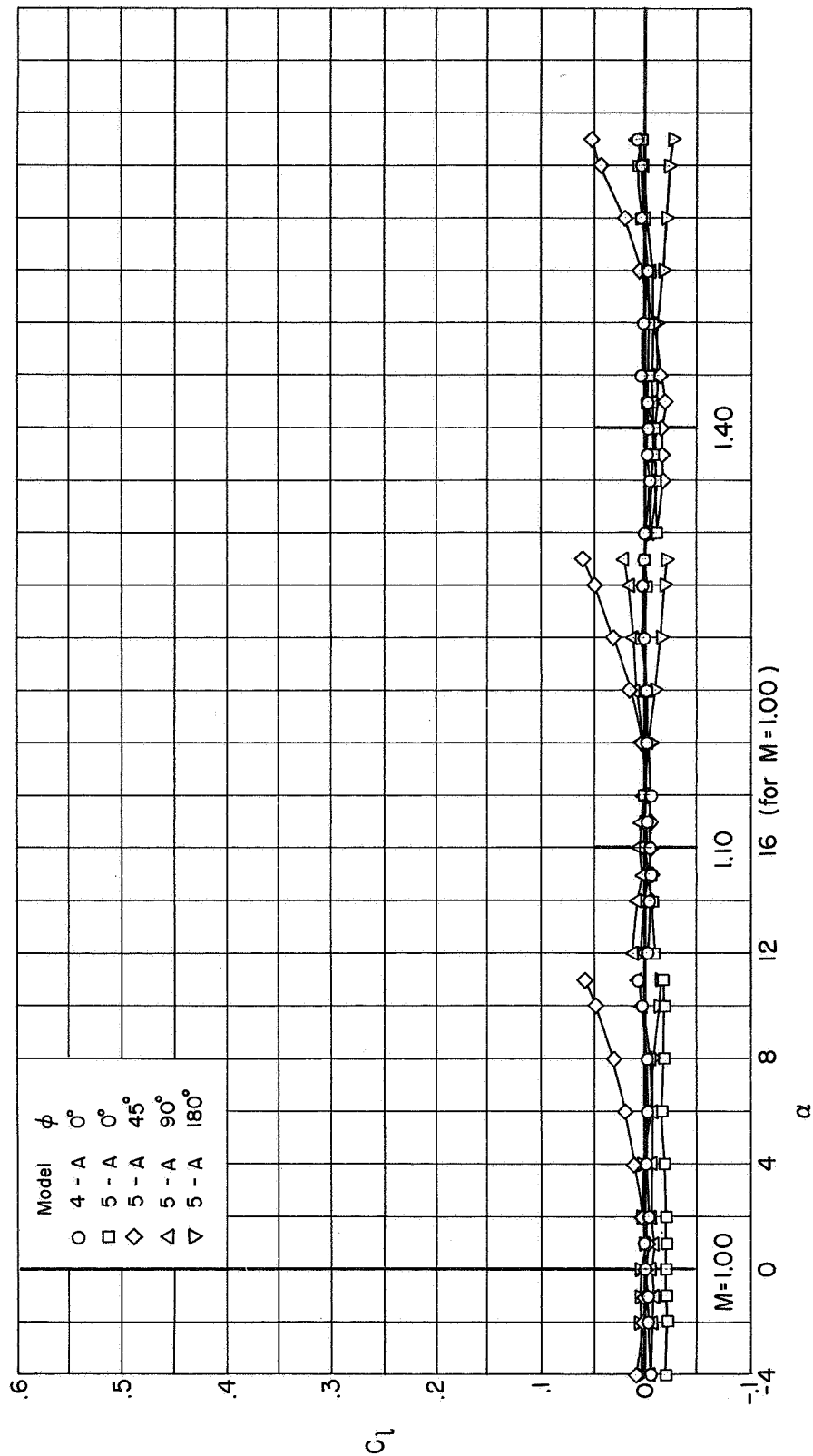
(b) $M = 1.00$ to 1.40

Figure 20.- Concluded.



(a) $M = 0.40$ to 0.90

Figure 21.- Effect of asymmetric protuberances and model roll angle on the variation of rolling moment coefficient for rocket assembly models.



(b) $M = 1.00$ to 1.40

Figure 21.- Concluded.

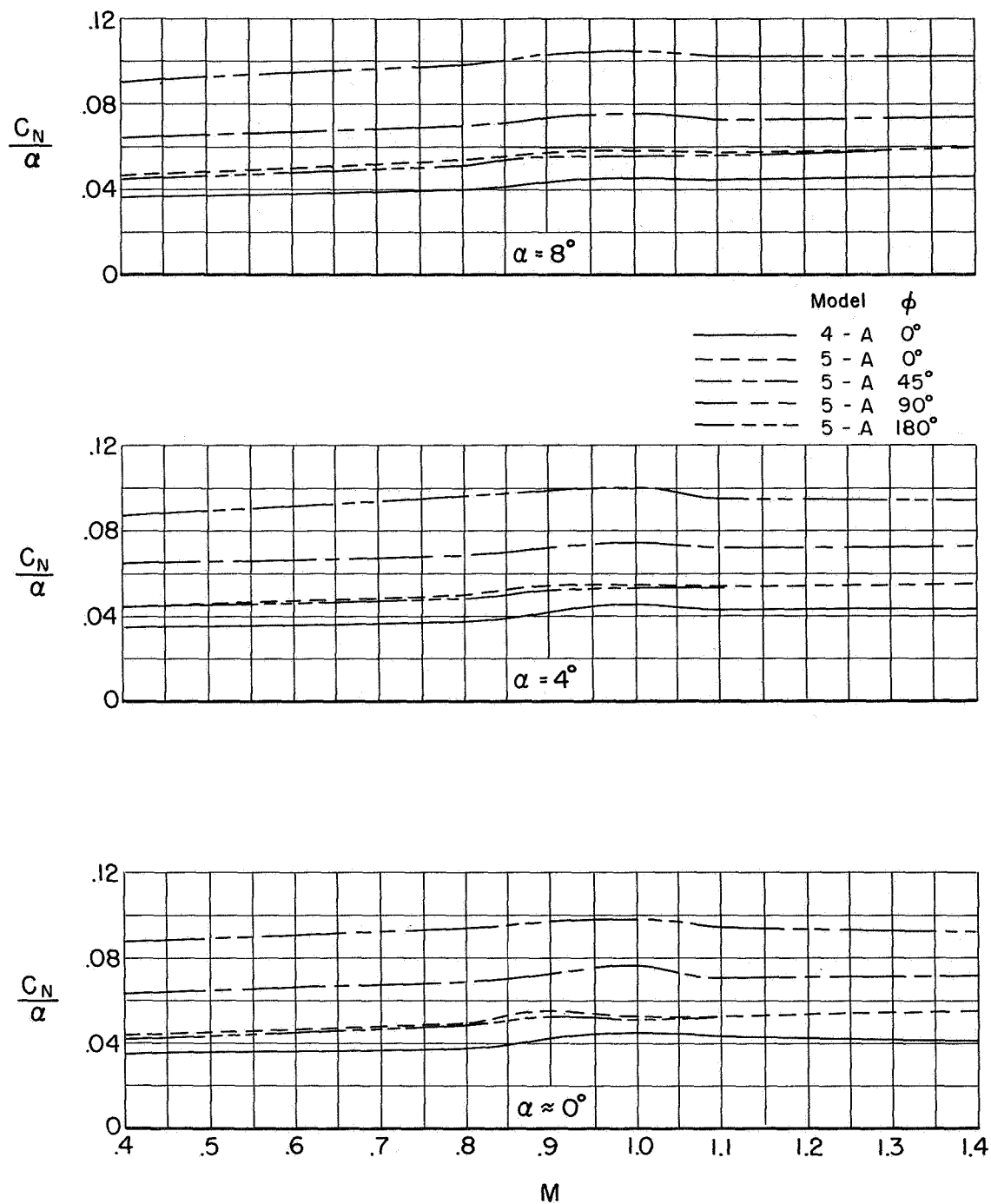


Figure 22.- Effect of asymmetric protuberances and model roll angle on the variation of normal-force parameter at selected angles of attack for rocket assembly models.

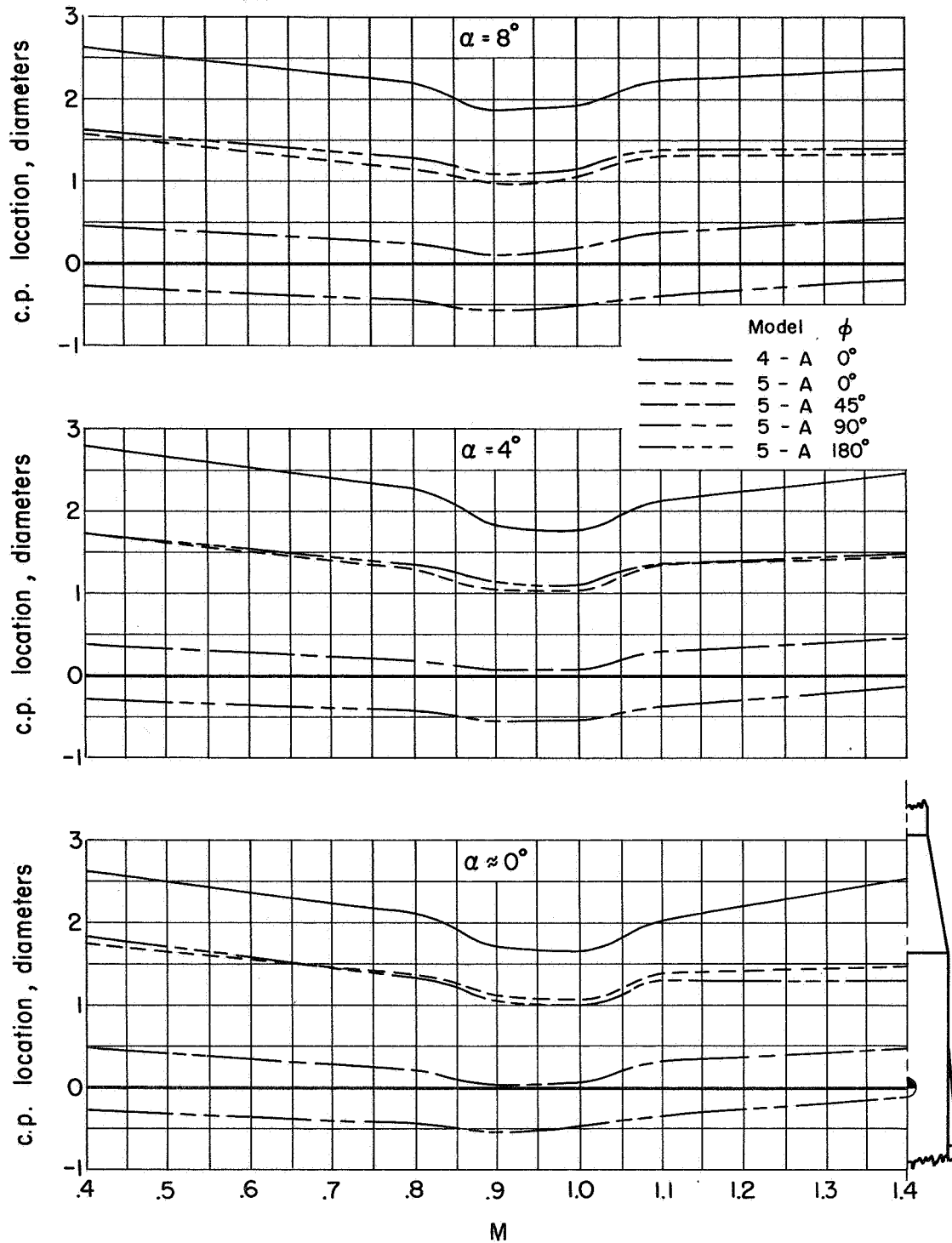


Figure 23.- Effect of asymmetric protuberances and model roll angle on the variation of center of pressure at selected angles of attack for rocket assembly models.

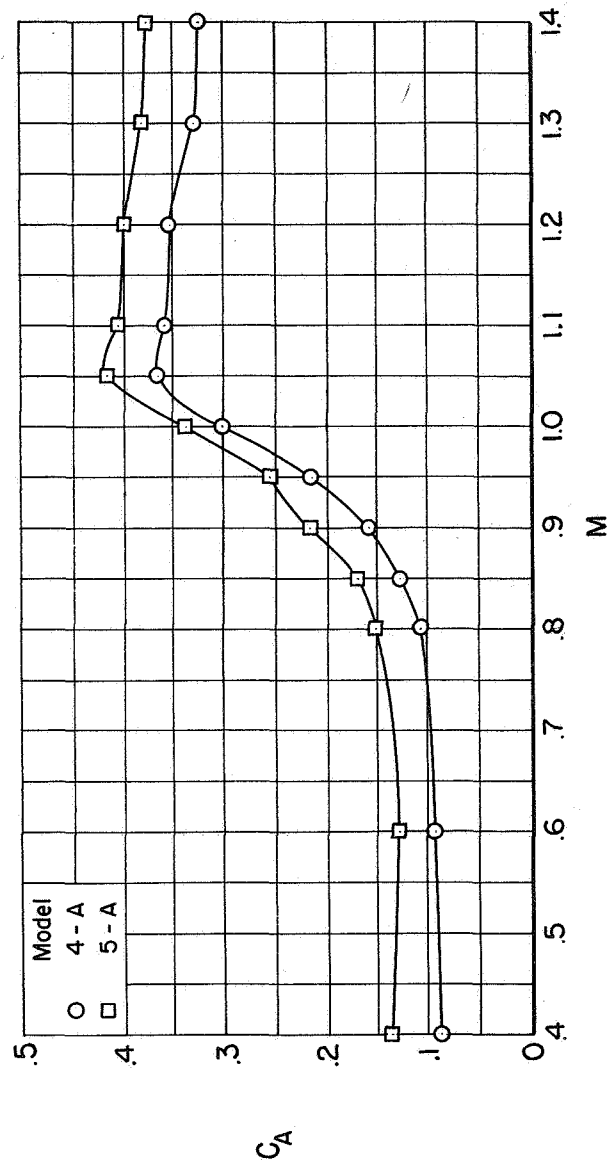


Figure 24.- Effect of asymmetric protuberances on the variation of axial-force coefficient at zero angle of attack for rocket assembly models.